Mapping the spatial distribution of NO_2 with in situ and remote sensing instruments during the Munich NO_2 imaging campaign

Gerrit Kuhlmann[1], **Ka Lok Chan**[2,3,a], **Sebastian Donner**[4], **Ying Zhu**[2], **Marc Schwaerzel**[1,5], **Steffen Dörner**[4], **Jia Chen**[6], **Andreas Hueni**[7], **Duc Hai Nguyen**[6,b], **Alexander Damm**[7,8], **Annette Schütt**[2], **Florian Dietrich**[6], **Dominik Brunner**[1], **Cheng Liu**[9], **Brigitte Buchmann**[1], **Thomas Wagner**[4], and **Mark Wenig**[2]

[1]Swiss Federal Laboratories for Materials Science and Technology (Empa), Dübendorf, Switzerland
[2]Meteorological Institute, Ludwig Maximilian University (LMU), Munich, Germany
[3]Remote Sensing Technology Institute (IMF), German Aerospace Center (DLR), Oberpfaffenhofen, Germany
[4]Max Planck Institute for Chemistry (MPIC), Mainz, Germany
[5]Environmental Remote Sensing Laboratory, École Polytechnique Fédérale de Lausanne, Lausanne, Switzerland
[6]Environmental Sensing and Modeling, Technical University of Munich (TUM), Munich, Germany
[7]Department of Geography, University of Zurich (UZH), Zurich, Switzerland
[8]Swiss Federal Institute of Aquatic Science and Technology (Eawag), Dübendorf, Switzerland
[9]Department of Precision Machinery and Precision Instrumentation,
University of Science and Technology of China (USTC), Hefei, China
[a]now at: Rutherford Appleton Laboratory Space, Harwell Oxford, United Kingdom
[b]now at: Leibniz Supercomputing Centre (LRZ), Garching bei München, Germany

Correspondence: Gerrit Kuhlmann (gerrit.kuhlmann@empa.ch)

Abstract. We present results from the Munich Nitrogen dioxide (NO_2) Imaging Campaign (MuNIC), where NO_2 near-surface concentrations (NSCs) and vertical column densities (VCDs) were measured with stationary, mobile, and airborne in situ and remote sensing instruments in Munich, Germany. The most intensive day of the campaign was 7 July 2016, when the NO_2 VCD field was mapped with the Airborne Prism Experiment (APEX) imaging spectrometer. The spatial distribution of APEX VCDs was rather smooth, with a horizontal gradient between lower values upwind and higher values downwind of the city center. The NO_2 map had no pronounced source signatures except for the plumes of two combined heat and power (CHP) plants. The APEX VCDs have a fair correlation with mobile multi-axis differential optical absorption spectroscopy (MAX-DOAS) observations from two vehicles conducted on the same afternoon ($r = 0.55$). In contrast to the VCDs, mobile NSC measurements revealed high spatial and temporal variability along the roads, with the highest values in congested areas and tunnels. The NO_x emissions of the two CHP plants were estimated from the APEX observations using a mass-balance approach. The NO_x emission estimates are consistent with CO_2 emissions determined from two ground-based Fourier transform infrared (FTIR) instruments operated near one CHP plant. The estimates are higher than the reported emissions but are probably overestimated because the uncertainties are large, as conditions were unstable and convective with low and highly variable wind speeds. Under such conditions, the application of mass-balance approaches is problematic because they assume steady-state conditions. We conclude that airborne imaging spectrometers are well suited for mapping the spatial distribution of NO_2 VCDs over large areas. The emission plumes of point sources can be detected in the APEX observations, but accurate flow fields are essential for estimating emissions with sufficient accuracy. The application of airborne imaging spectrometers for studying NSCs is less straightforward and requires us to account for the non-trivial relationship between VCDs and NSCs.

1 Introduction

Nitrogen oxides (NO$_x$ = NO + NO$_2$) are important precursors of ozone and particulate matter and thus play an important role in the formation of photochemical smog. Except for close to the source, NO$_2$ is usually the dominant component of NO$_x$ and is also the more critical species in terms of health effects (Beelen et al., 2014; Brunekreef and Holgate, 2002). Because of their negative effects on health, NO$_2$ concentration levels are limited by air pollution legislation, but these limits are still frequently exceeded in urban areas (European Environment Agency, 2019; World Health Organization, 2021). NO$_x$ is mainly emitted by road traffic but also by residential heating, industrial facilities, power plants and some other combustion sources. Because of these localized emissions and the relatively short lifetime of NO$_2$, NO$_2$ concentrations have a high spatial and temporal variability, making high-resolution NO$_2$ maps an important tool for urban air pollution control and epidemiological studies (Maiheu et al., 2017).

NO$_2$ maps can be created in different ways, each with its specific advantages and disadvantages: in situ ground measurements can be combined with geostatistical methods such as land-use-regression models to generate city-wide air pollution maps (e.g., Mueller et al., 2015), but urban air quality monitoring networks are typically very sparse, limiting the accuracy of such maps, although mobile sensors on public buses or trams could increase the measurement density (e.g., Hagemann et al., 2014; Hundt et al., 2018). Dense networks of low-cost sensors have also been proposed as a complement to the traditional networks, but issues with precision, stability, or specificity of existing sensors remain an obstacle to their widespread deployment (Heimann et al., 2015; Bigi et al., 2018; Karagulian et al., 2019). As an alternative, networks of ground-based remote sensing instruments including multi-axis differential optical absorption spectroscopy (MAX-DOAS) (Leigh et al., 2007) and tomographic long-path (LP) DOAS systems (Platt et al., 2009) can be used to retrieve NO$_2$ maps. The disadvantage of this method is that a high spatial resolution can only be achieved with a very large number of light paths, making a city-wide network expensive. Furthermore, the resulting NO$_2$ maps mainly represent concentrations above buildings and are not near the ground. A third option is the use of imaging spectrometers on satellites and aircraft. Current satellite instruments have spatial resolutions down to a few kilometers, which is still too coarse for resolving NO$_2$ in a city. However, satellite instruments have been shown to be capable of observing the downwind plume of large cities (e.g., Beirle et al., 2011, 2019; Lorente et al., 2019). In contrast, airborne imaging spectrometers have inherently much higher spatial resolutions of a few tens of meters and thus can retrieve detailed NO$_2$ maps for whole cities (Heue et al., 2008; Lawrence et al., 2015; Popp et al., 2012; Schönhardt et al., 2015; Tack et al., 2017; Nowlan et al., 2016; Tack et al., 2019). However, satellite and airborne instruments measure (tropospheric) vertical column densities (VCDs), while near-surface concentrations (NSCs) are the quantity of interest for the assessment of air pollution exposure. Since the linkage between VCDs and NSCs is variable and depends on various factors (e.g., topography, emission sources, and meteorological data), algorithms have been developed to transfer VCDs to NSCs for satellite observations using statistical models trained with NO$_2$ monitoring networks (e.g., Xu et al., 2019; de Hoogh et al., 2019; Kim et al., 2021).

These algorithms require large training datasets and cannot be applied to airborne measurement campaigns as typical urban monitoring networks are too small to train the relationship between VCDs and NSCs from a single measurement flight. This limits the current capacity to reliably retrieve NSCs and to study the spatial variability of NO$_2$ and its sources in cities with airborne remote sensing observations. We therefore conducted the Munich NO$_2$ Imaging Campaign (MuNIC) to validate airborne imaging spectrometers with ground-based observations and to collect data for advancing understanding of the relationship between VCDs and NSCs in Munich, Germany. We collected data with the Airborne Prism EXperiment (APEX) imaging spectrometer (Schaepman et al., 2015) and measured NO$_2$ VCDs and NSCs using mobile (MAX-DOAS, cavity-attenuated phase-shift (CAPS), CE-DOAS) and stationary instruments (LP-DOAS, MAX-DOAS) as well as meteorological and other related parameters. In this paper, we validate the APEX NO$_2$ map using the mobile MAX-DOAS observations, analyze the consistency and relationship between NO$_2$ VCDs and NSCs, and demonstrate the applicability of the collected data to estimate the emissions of the two largest point sources in the city.

2 Data and method

The MuNIC campaign was conducted from 1 to 13 July 2016 in Munich, Germany (48.1375° N, 11.575° E), measuring NO$_2$ NSCs and VCDs with stationary, mobile and airborne instruments (Fig. 1; Table 1). The most intensive day of the campaign was 7 July, when a map of tropospheric NO$_2$ VCDs was retrieved with the APEX imaging spectrometer. On the same day, NO$_2$ NSCs and VCDs were measured with two vehicles from the Ludwig Maximilian University of Munich (LMU) and the Max Planck Institute for Chemistry (MPIC). Both vehicles were equipped with NO$_2$ in situ monitors and mobile MAX-DOAS instruments for measuring NSCs and VCDs, respectively. In addition, stationary measurements were conducted at LMU's Meteorological Institute Munich (MIM) near the city center, at the Oscar-von-Miller (OvM) tower northeast of Munich, and near the Munich South combined heat and power (CHP) plant. In the following, the different measurements are described in more detail.

Table 1. Instruments and their measurements available during MuNIC on 7 July 2016.

Instrument	Operators	Parameters	Measurement locations	Measurement times (UTC)
APEX	Empa, UZH	Trop. NO$_2$ VCDs, HCRF	DLR aircraft	12:16–12:56
Mini MAX-DOAS	MPIC	Trop. NO$_2$ VCDs	LMU vehicle	07:50–09:55, 11:30–15:30
Tube MAX-DOAS	MPIC	Trop. NO$_2$ VCDs	MPIC vehicle	08:00–09:45, 11:15–15:30
CE-DOAS	LMU	NO$_2$ NSCs	MPIC vehicle	08:10–09:40, 11:30–15:30
CAPS	Empa	NO$_2$ NSCs	LMU vehicle	07:50–09:55, 11:15–15:30
MAX-DOAS (OvM)	LMU, USTC	NO$_2$ profiles	OvM tower	None
MAX-DOAS (MIM)	LMU	NO$_2$ profiles	MIM roof	06:56–16:10
LP-DOAS	LMU	NO$_2$ NSCs	MIM roof	All day
Bruker EM27/SUN FTIRs	TUM	XCO$_2$, XCH$_4$	Munich South CHP plant	09:20–16:10
ASD	Empa, LMU, UZH	HCRF	Handheld	09:00–14:30

2.1 Meteorological observations

Meteorological parameters were measured every minute at the MIM and the OvM tower at different altitudes. Air temperature, air pressure, wind speed and direction, and global radiation are available. Wind speeds and directions were measured on the MIM's rooftop at 30 m above ground. At the OvM tower, temperature and wind speeds were measured at 2, 5, 10, 20, 35, and 50 m above ground as well as wind directions at 10 and 50 m. Wind information is also available from measurements at the Munich South CHP plant site at 15 m above ground and from the COSMO-1 and COSMO-7 model analysis products of the Swiss Federal Office of Meteorology and Climatology (MeteoSwiss).

2.2 Monitoring stations

The Bavarian Landesamt für Umwelt (LfU) is operating a network of five monitoring stations in Munich (Fig. 1) measuring hourly concentrations of several air pollutants including NO$_2$ and meteorological parameters. The network consists of two suburban background stations (Allach and Johanneskirchen), one urban background station (Lothstraße), and two urban roadside stations (Landshuter Allee and Stachus). NO$_2$ is measured with standard chemiluminescence NO$_x$ analyzers, which use heated molybdenum catalysts to convert NO$_2$ to NO before detection.

2.3 LP-DOAS

A long-path DOAS system was installed on the MIM's rooftop at 25 m above ground. The system measures the mean NO$_2$ concentrations along optical paths between the instrument and retro-reflectors installed at neighboring buildings using a blue light-emitting diode (LED). The sampling time ranges from 30 to 90 s depending on visibility conditions. The measurement setup and the NO$_2$ retrieval are described in detail by Zhu et al. (2020). Three optical paths were operated during the campaign (Fig. S1 in the Supplement): a 816 m path to the rooftop of the N5 building of the Technical University of Munich (TUM) with the retro-reflector installed at 28 m above ground, a 2174 m path to the rooftop of the LMU physics building at 28 m above ground, and a 3828 m path to the rooftop of the Hilton hotel building at 48 m height. The light paths cover the university campus, a public park, residential areas, and several roads.

2.4 Stationary MAX-DOAS

NO$_2$ profiles above roof level were measured with a MAX-DOAS instrument at the MIM's rooftop in the city center and a second MAX-DOAS instrument on top of the OvM tower about 15 km northeast of the city center. Unfortunately, no measurements are available at the OvM tower for 7 July 2016 due to technical issues of the instrument.

The MAX-DOAS was programmed to measure scattered solar radiances at nine elevation angles (2, 3, 4, 5, 6, 8, 15, 30, and 90°) and seven azimuth angles (0, 90, 135, 180, 225, 270, and 315°). In this study, only measurements at an azimuth angle of 0° (pointing northwards) were analyzed, from which differential NO$_2$ slant columns (dSCDs) were retrieved using a DOAS analysis for a wavelength range from 425 to 490 nm. The DOAS analysis considered NO$_2$, O$_4$, O$_3$, and H$_2$O absorption cross sections, a Ring spectrum, as well as a polynomial of degree 5. Small shift and squeeze of the wavelength are allowed in the wavelength mapping process to compensate for small uncertainties caused by the instability of the spectrograph.

Aerosol extinction coefficient profiles were retrieved from the O$_4$ absorption bands at 477 nm using the Munich Multiple wavelength MAX-DOAS retrieval algorithm (M^3), described in detail in Chan et al. (2018, 2019, 2020). Due to the systematic discrepancy between observation and model simulation of O$_4$ DSCDs (e.g., Wagner et al., 2009), all MAX-DOAS observations of O$_4$ DSCDs are multiplied by a correction factor of 0.8 (see Chan et al., 2019, for details). The algorithm uses the optimal estimation method (Rodgers, 2000) and the libRadtran radiative transfer code as the forward model (Mayer and Kylling, 2005; Emde et al., 2016). The aerosol profiles obtained from the procedure are used for the calculation of air mass factors for discrete vertical lay-
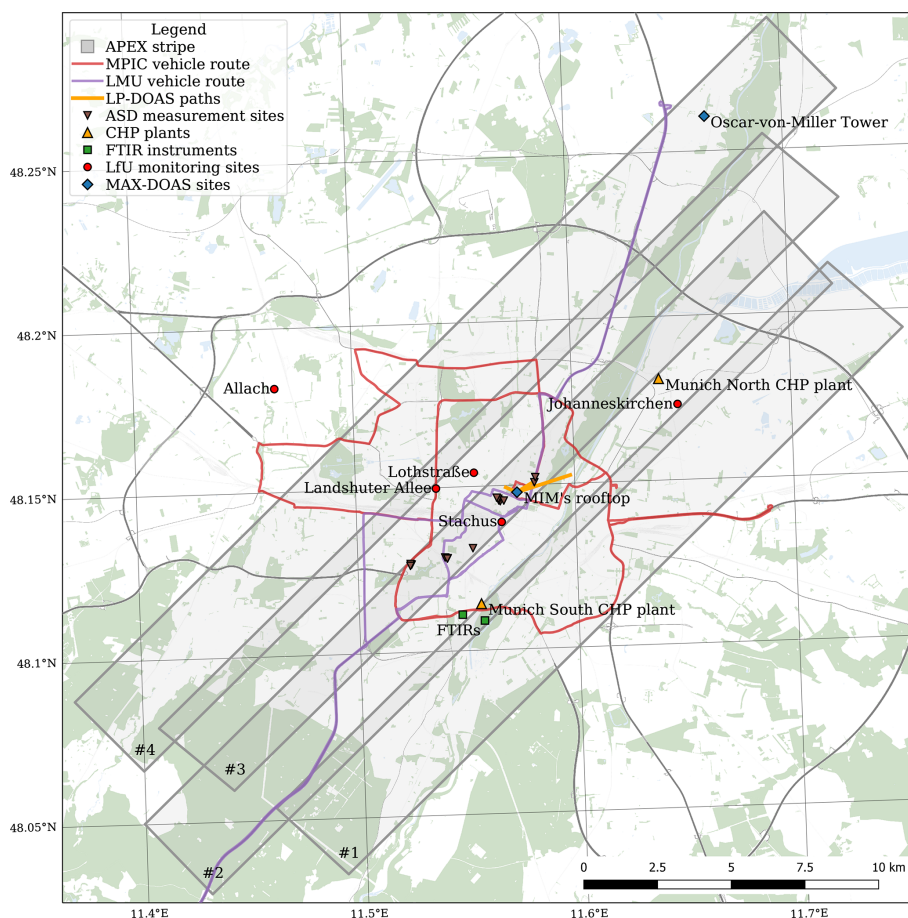
Figure 1. Map of Munich with overlaid APEX flight stripes (nos. 1–4), routes taken by the LMU and MPIC vehicles in the afternoon of 7 July 2016, as well as locations of combined heat and power (CHP) plants, Fourier transform infrared (FTIR) instruments, LfU monitoring sites, and stationary MAX-DOAS instruments and the locations of surface reflectance measurements with the ASD instruments. Map data from © OpenStreetMap contributors 2021. Distributed under the Open Data Commons Open Database License (ODbL) v1.0.

ers (1D-layer AMFs) required for NO₂ profile inversion. The layer AMFs are calculated at 477 nm for the retrieval of NO₂ profiles using the Monte Carlo solver (MYSTIC) of libRad-tran (Emde et al., 2016; Schwaerzel et al., 2020).

2.5 Airborne Prism Experiment (APEX)

APEX is a push-broom imaging spectrometer that has been developed for environmental monitoring (Schaepman et al., 2015). It measures radiance spectra with an optimized integration time simultaneously in 1000 across-track spatial pixels within a 28° field of view. At a flight altitude of 7360 m above ground, its spatial resolution is about 4 m × 6 m in the across- and along-track directions, respectively. The along-track resolution is computed from aircraft altitude, ground speed, and integration time. For each pixel, spectral radiance is measured in the visible and near-infrared (VNIR, 372–1015 nm) and shortwave infrared (SWIR, 940–2540 nm) channels. To retrieve NO₂ VCDs, spectra were acquired in the unbinned mode, providing the highest nominal spectral

resolution of 0.86 nm full width at half maximum (FWHM) and 0.45 nm spectral sampling interval (SSI) in the VNIR channel with 334 spectral bands. Note that FWHM and SSI vary with wavelength and range from 0.86 to 15 nm (FWHM) and from 0.45 to 7.5 nm (SSI), owing to the dispersion characteristics of the VNIR prism.

The APEX measurements were acquired along four predefined stripes shown in Fig. 1 on 7 July 2016 in the early afternoon (14:16–14:56 CEST). The four stripes cover a large fraction of the city, with a large overlap between the stripes to increase the number of APEX observations in the city center, where most ground-based observations were conducted. In addition, the stripes cover forest and agriculture land, which were used as background spectra in the DOAS retrieval.

APEX NO₂ retrieval algorithms were developed at Empa in Switzerland (Popp et al., 2012) and at BIRA in Belgium (Tack et al., 2017) using the QDOAS software for the DOAS analysis and the LIDORT radiative transfer model for AMF computations. In this study, we used a new version of the Empa APEX NO₂ retrieval algorithm, which has been com-

pletely rewritten using Python, allowing for automatic and parallel processing of APEX measurements. The new version uses the Python library flexDOAS for the DOAS analysis (Kuhlmann, 2022) and the Monte Carlo MYSTIC solver for AMFs (Schwaerzel et al., 2020).

To increase the signal-to-noise ratio for the NO$_2$ retrieval, 20×10 APEX pixels were spatially binned in the across- and along-track directions, respectively. As a result, the spatial resolution of the APEX instrument is reduced to about $80\,\mathrm{m} \times 60\,\mathrm{m}$. An in-flight spectral calibration was conducted to improve the accuracy of center wavelength positions and the FWHM of the instrument's slit function (Kuhlmann et al., 2016). This was required because the default spectral calibration provided by the APEX processing and archiving facility (Hueni et al., 2009, 2013) was not sufficiently accurate for the retrieval of NO$_2$.

NO$_2$ dSCDs were retrieved from the spatially binned APEX spectra using flexDOAS. The last 50 spectra at the western end of each stripe were used as a reference spectrum for each across-track position. The DOAS analysis was applied to a window from 470 to 510 nm where we fitted NO$_2$ and O$_4$ absorption cross sections, a Ring spectrum, a five-degree polynomial, as well as a relative offset fitted as a quadratic polynomial that was subtracted from both the measurement and reference spectra. The cross sections of O$_3$ and H$_2$O are not considered due to cross-correlations and overparameterization in the small fitting window (Popp et al., 2012; Tack et al., 2017).

The NO$_2$ dSCDs are the differences between SCDs in the observation and reference spectra,

$$\mathrm{dSCD} = \mathrm{SCD} - \mathrm{SCD_{ref}}, \tag{1}$$

which are solved for tropospheric VCDs using $\mathrm{SCD} = \mathrm{AMF} \cdot \mathrm{VCD}$ as

$$\mathrm{VCD} = \frac{\mathrm{dSCD} + \mathrm{VCD_{ref}} \cdot \mathrm{AMF_{ref}}}{\mathrm{AMF}}, \tag{2}$$

where VCD$_{\mathrm{ref}}$ and AMF$_{\mathrm{ref}}$ are the reference VCDs and AMFs for each across-track position. Mobile MAX-DOAS observations conducted in the reference area during the APEX flight were used as reference VCDs (VCD$_{\mathrm{ref}}$).

To calculate the AMFs, 1D-layer AMFs were computed with the MYSTIC solver of the libRadtran model (Emde et al., 2016; Schwaerzel et al., 2020) depending on Sun position, instrument viewing direction, surface reflectance, surface elevation, and atmospheric scattering by molecules and aerosols using a US standard atmosphere. Surface reflectances were taken from the APEX surface reflectance product at 490 nm (cf. Sect. 2.8) in the center of the DOAS fitting window assuming Lambertian equivalent reflectance (LER). Aerosol scattering was included using an aerosol optical depth of 0.10 measured by the AERONET station on the MIM's rooftop and libRadtran's default aerosol profile. Total AMFs were computed from the 1D-layer AMFs using

the NO$_2$ profile measured by the MAX-DOAS instrument on the MIM's rooftop.

The APEX NO$_2$ VCDs were destriped to account for small variations of dSCDs and true VCD$_{\mathrm{ref}}$ in the across-track direction by subtracting deviations from a cubic polynomial fitted to the mean across-track VCDs. In addition, we performed a bias correction between the different aircraft overpasses by adding a constant offset to each stripe so that the mean values of the overlapping parts of two neighboring stripes are identical. Both the across-track variations as well as the difference between stripes are mainly caused by differences in spectral and radiometric calibration (Kuhlmann et al., 2016). The NO$_2$ VCDs were then mapped onto a longitude–latitude grid with about 10 m resolution for comparison with the ground-based observations using the gridding algorithm of Kuhlmann et al. (2014) (Code repository: Kuhlmann, 2021b).

The uncertainties in NO$_2$ VCDs were calculated as the quadratic sum of the uncertainties in dSCDs, AMFs, and SCD$_{\mathrm{ref}}$:

$$\sigma_{\mathrm{VCD}} = \sqrt{\left(\frac{\sigma_{\mathrm{dSCD}}}{\mathrm{AMF}}\right)^2 + \left(\frac{\sigma_{\mathrm{SCD_{ref}}}}{\mathrm{AMF}}\right)^2 + \sigma_{\mathrm{AMF}}^2 \left(\frac{\mathrm{VCD}}{\mathrm{AMF}}\right)^2}, \tag{3}$$

where σ_{dSCD} was estimated from the DOAS analysis. The uncertainties in AMFs and SCD$_{\mathrm{ref}}$ were estimated from the comparison with the ground-based remote sensing observations conducted during the campaign.

2.6 Mobile measurements

Mobile measurements were conducted with two vehicles operated by MPIC and LMU, respectively. Each vehicle was equipped with an in situ instrument measuring near-surface concentrations (CE-DOAS and CAPS) and a spectrometer measuring NO$_2$ column densities (Tube and Mini MAX-DOAS) (see Table 1). The measurements were conducted along varying routes in the city. The MPIC vehicle mostly drove circles in the city center to capture the NO$_2$ fields in across-track direction of the APEX measurements, while the LMU vehicle drove from the southwest to the northeast of the city along the highway or on smaller roads in the city center to sample in the along-track direction of APEX.

2.6.1 Mobile in situ instruments

Near-surface NO$_2$ concentrations were measured with two highly sensitive and specific in situ instruments: first a T500U CAPS NO$_2$ analyzer from Teledyne API that is routinely used in the Swiss National Air Pollution Monitoring Network (NABEL). CAPS consists of a blue LED, a measurement chamber with two highly reflective mirrors, and a vacuum photodiode detector. The instrument uses the CAPS technique to directly measure NO$_2$ (Kebabian et al., 2005, 2008). CAPS was installed in the LMU vehicle with

the sample inlet fixed at the roof of the vehicle at about 2 m height. The NO$_2$ concentrations were recorded every 2 s.

The second instrument applied broadband cavity enhanced differential optical absorption spectroscopy (CE-DOAS), which uses a blue LED, a measurement chamber, and a spectrometer to obtain NO$_2$ concentrations using the DOAS technique between 435.6 and 455.1 nm (Platt et al., 2009; Zhu et al., 2020). The CE-DOAS was installed in the MPIC vehicle with the inlet located at the front right window of the vehicle at 1.5 m above the ground, and measurements were recorded every 2 s.

CAPS and CE-DOAS agreed well when operated together on the LMU vehicle on 1 and 4 July 2016. Pearson correlation coefficients were 0.995 and 0.984, and root mean square errors (RMSEs) were 6.1 and 5.9 ppbv on the two days. The differences between CAPS and CE-DOAS are due to instrument differences such as length of tubing and integration times, the short measurement interval of 2 s, and the high variability of NO$_2$ concentrations on roads. Furthermore, it was necessary to shift CAPS measurements by 16.9 and 5.6 s, respectively (Fig. S2). The time differences were caused by non-synchronized computer clocks and the differences in tubing and integration times. On campaign day, GPS times were used to minimize time differences between instruments.

2.6.2 Mobile MAX-DOAS measurements

The mobile MAX-DOAS measurements were carried out using two instruments operated by MPIC: the Tube MAX-DOAS, which was mounted on the MPIC vehicle, is a scientific grade instrument with a high signal-to-noise ratio and stable spectroscopic properties (see, e.g., Kreher et al., 2020). The Mini MAX-DOAS is a more compact instrument but with a lower signal-to-noise ratio and less stable spectral properties (see, e.g., Shaiganfar et al., 2011). This instrument was mounted on the LMU vehicle. Because of the different signal-to-noise ratios, the total integration times for individual measurements were set to 30 s for the Tube MAX-DOAS and 60 s for the Mini MAX-DOAS instruments, respectively. The obtained spectra are averages of multiple single measurements with integration times adjusted according to current sky conditions. Mean individual integration times were roughly 65 ms, leading to numbers of scans of roughly 460 and 920 for the two instruments, respectively. One complete elevation sequence contained six (Tube MAX-DOAS) or seven (Mini MAX-DOAS) measurements at a low (22°) elevation angle, followed by one measurement in the zenith direction. The line of sight of the Mini MAX-DOAS instrument was in the driving direction and the one of the Tube MAX-DOAS instrument was directed backwards with respect to the driving direction. NO$_2$ was analyzed in the spectral range from 400 to 439 nm using a fixed daily Fraunhofer reference measured in the zenith direction. Only results with root mean square (rms) values below 8×10^{-4} (Tube MAX-

DOAS) and below 2×10^{-3} (Mini MAX-DOAS) were considered for further processing. The method described in Wagner et al. (2010) and Ibrahim et al. (2010) was applied to determine the NO$_2$ absorption in the Fraunhofer reference spectrum and to correct for the changing stratospheric NO$_2$ absorption.

2.7 Fourier transform infrared (FTIR) spectrometers

Two ground-based FTIR spectrometers were deployed near the Munich South CHP plant to measure column-averaged dry air mole fractions of CO$_2$ and CH$_4$ (XCO$_2$ and XCH$_4$). The instruments are owned by the Karlsruhe Institute of Technology (KIT) and Technical University of Munich (TUM) and are identified as EM27 KIT and EM27 TUM, respectively. Both instruments are operated by TUM.

The compact and mobile solar-tracking FTIR spectrometers (Bruker EM27/SUN, Gisi et al., 2012) point towards the Sun during measurements and measure spectra in the wavenumber range from 6000 to 9000 cm^{-1}. By placing one spectrometer upwind and the other downwind of the CHP plant, differential column measurements (DCMs) can be used to determine the CO$_2$ and CH$_4$ emissions from this source. DCMs have proven to be an effective method for determining emissions from different types of sources (Hase et al., 2015; Chen et al., 2016; Dietrich et al., 2021; Toja-Silva et al., 2017; Zhao et al., 2019). Differential column measurements exhibit a very high precision of 0.01 % for XCO$_2$ and XCH$_4$ at a 10 min integration time (Chen et al., 2016; Hedelius et al., 2016).

To capture the emission plume, the spectrometers were placed based on the forecasted wind direction. On 7 July 2016, the wind was blowing from the northwest in the morning, turning to northeast in the afternoon. One spectrometer was placed southwest of the CHP plant to capture the plume in the morning and the other spectrometer south to capture the plume at noon. As a result, the stations acted alternately as downwind sites and as background sites throughout the day.

2.8 Surface reflectance

Surface reflectance is a critical input parameter for the AMF computation, because uncertainties in the reflectance can have a strong impact on the NO$_2$ VCDs. The APEX reflectance product calculates hemispheric–conical reflectance factors (HCRFs; Schaepman-Strub et al., 2006) using the atmospheric correction software ATCOR-4 (Richter and Schläpfer, 2002). In short, atmospheric water vapor and aerosol optical depth are estimated from APEX radiance data, which are used, together with other parameters describing the Sun-observer geometry, to obtain representative atmospheric transfer functions (e.g., transmittance, spherical albedo, path radiance). The transfer functions were precalculated with MODTRAN-5 (Berk et al., 2005) and stored
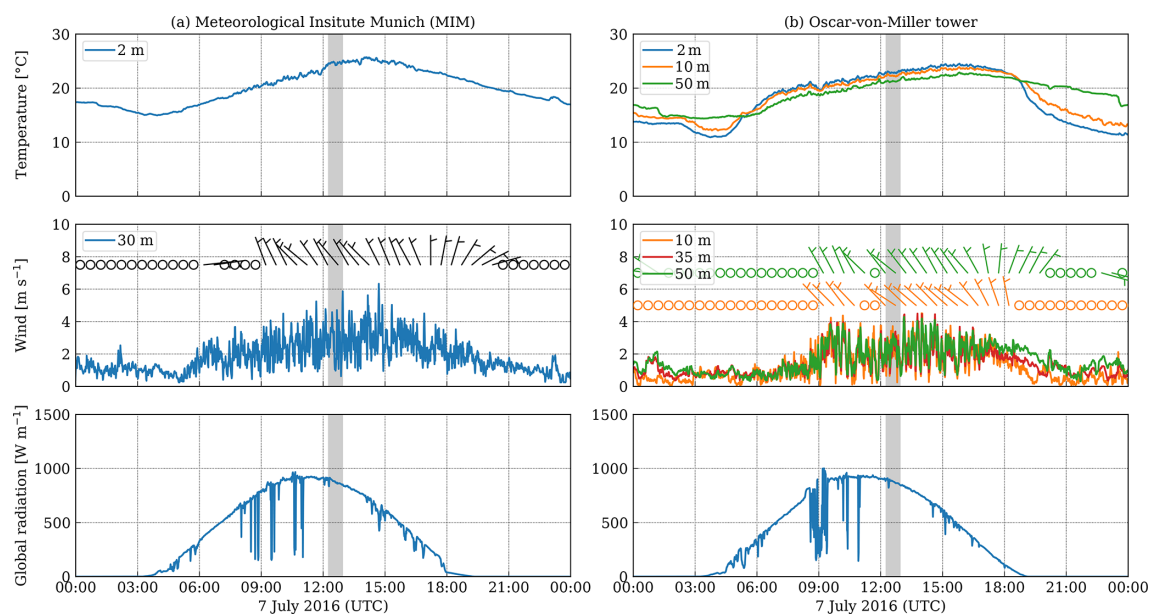
Figure 2. Time series of meteorological observations (temperature, wind speed and direction, and global radiation) at **(a)** the Meteorological Institute Munich (MIM) and at **(b)** the Oscar-von-Miller (OvM) tower. The APEX flight time is shown as a gray area.

in a look-up table. Radiance data are also used to estimate spectral non-uniformities (e.g., spectral shift, band broadening). This information is essential to spectrally convolve identified atmospheric transfer functions and eventually retrieve HCRFs.

To evaluate the APEX surface reflectance product, HCRF spectra were collected with a handheld analytical spectral device (ASD) field spectroradiometer during the campaign. In total, 14 spectra were measured on 7 July 2016 from 11:05 to 16:19 CEST. All ASD measurements were located in the second and third APEX stripes and included surfaces of varying types and brightnesses. The locations are shown in Fig. 1, and details are listed in Table S1.

3 Results

3.1 Campaign day with APEX overpass

The APEX flight window was part of a larger measurement campaign in June and July 2016 with various targets. The choice of a suitable day for Munich is based mainly on flight permission and weather conditions. The first 2 weeks of July 2016 were mostly cloudy, with daily mean temperatures and wind speeds ranging from 12 to 27 °C and from 1.0 to 3.9 m s⁻¹, respectively. A favorable situation with almost no clouds was predicted for 7 July 2016 for the area of Munich, which allowed us to conduct the APEX measurements in the early afternoon (14:16–14:56 CEST).

Figure 2 shows the time series of meteorological parameters (temperature, wind speed and direction, and global radiation) measured at MIM and at the OvM tower on this day.

In the morning, small cumulus clouds were still present over Munich, which can be seen as a reduction in global radiation. In the afternoon, the clouds mostly vanished, making it possible to conduct the APEX flight. Figure S3 shows the true color composite of the APEX measurements, showing only a small cloud at the edges of the image.

Wind speeds were low during night (about 1 m s⁻¹) and slightly higher and highly variable during the day (1 to 6 m s⁻¹). The wind directions were mostly northwesterly during day, turning to northeasterly in the evening. We estimated the dispersion category during daytime as very unstable (category V) based on the procedure published by the Association of German Engineers, which determines dispersion categories based on tabulated values for wind speed, cloud fraction, and hour of day (VDI – Fachbereich Umweltmeteorologie, 2009, Annex A). Wind speed and direction are consistent with the simulations from the COSMO-1 and COSMO-7 analysis products provided by MeteoSwiss with 1 and 7 km spatial resolution, respectively (Fig. S11). The COSMO-1 model with about 1 km resolution shows small convective cells with highly variable 10 m wind speeds over Munich with a similar spatial variability to the temporal variability of the ground measurements.

Figure 3a shows the time series of NO₂ NSCs at the monitoring stations on 7 July 2016. The NO₂ measurements show a morning peak during rush hour and an increase in the evening when the boundary layer becomes stable again, solar radiation is missing, and the sources (traffic) are still active. The APEX flight was performed around the time of the lowest NSCs. Concentrations were about 5 ppbv at the two suburban background stations (Allach and Johanneskirchen)
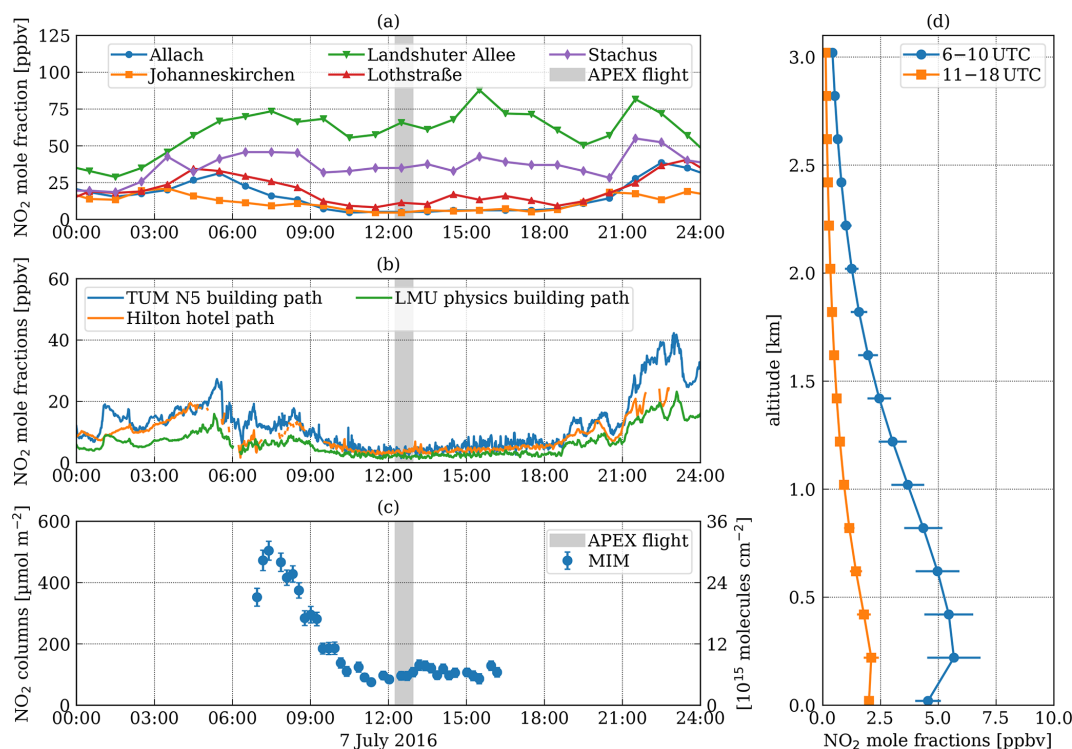
Figure 3. Time series of NO$_2$ mole fractions from **(a)** monitoring stations and **(b)** the LP-DOAS systems. **(c)** Time series of vertical column densities and **(d)** mean NO$_2$ profiles from the MAX-DOAS instrument on the MIM's rooftop on 7 July 2016.

and somewhat higher at 11 ppbv at the urban background station (Lothstraße). Different from these stations, the two urban traffic stations showed only little variations during the day due to their proximity to emission sources. Concentrations during the APEX flight were 35 and 66 ppbv at Stachus and Landshuter Allee, respectively. The LP-DOAS also measured the diurnal cycle with molar fractions similar to the suburban background stations due to the elevated light paths measuring NO$_2$ above the urban canopy. The LP-DOAS measured NO$_2$ concentrations of about 5 ppbv during the APEX overpass.

The MAX-DOAS instrument on the rooftop (Fig. 3c) measured the highest NO$_2$ VCDs in the early morning, with up to 504 μmol m^{-2}. NO$_2$ VCDs dropped substantially to about 104 ± 15 μmol m^{-2} in the afternoon. Note that 100 μmol m^{-2} is about 6×10^{15} molec. cm^{-2}. Since the temporal variability of NO$_2$ VCDs was small in the afternoon, differences between mobile and APEX measurements due to different measurement times are likely small.

Figure 3d shows averaged NO$_2$ profiles retrieved in the morning and in the afternoon. The profiles were retrieved for an azimuth angle of 0 degrees, i.e., looking northwards. The mole fractions in the lowest layer (0–200 m) were only 4.6 and 2.0 ppbv in the morning and afternoon, respectively, which is smaller than the 8.4 and 3.8 ppbv measured by the LP-DOAS system on average. The averaging kernels of MAX-DOAS retrieval for the lowest layer range between

0.85 and 1, indicating the retrieval reconstructs the lowest layer quite well. However, the lowest layer of MAX-DOAS represents the average of the lowest 200 m, while LP-DOAS measures at about 30 m above ground. Therefore, it is expected that LP-DOAS will measure higher concentrations than MAX-DOAS.

3.2 Mobile in situ measurements

Figure 4a shows the NO$_2$ mole fractions along the routes taken by the LMU and MPIC vehicles on 7 July 2016 in the afternoon. The markers for the LfU sites and lines for LP-DOAS show mean values in the afternoon (11:00–17:00 UTC). Figure 4b and c show the corresponding time series of NO$_2$ mole fractions. A corresponding figure showing measurements during the morning (07:00–10:00 UTC) is available in Fig. S4.

NO$_2$ mole fractions varied strongly along the route because they are very sensitive to local emissions. The values ranged from 0 to 890 ppb, with highest values being observed in congested areas, in front of traffic lights, or in tunnels. While 2 s values show high variability along the road, 30 min averages are similar to hourly measurements at the roadside stations at Stachus and Landshuter Allee when the vehicle passed at distances of 75 m and < 10 m from the stations, respectively (Fig. 4b and c). A more detailed comparison of
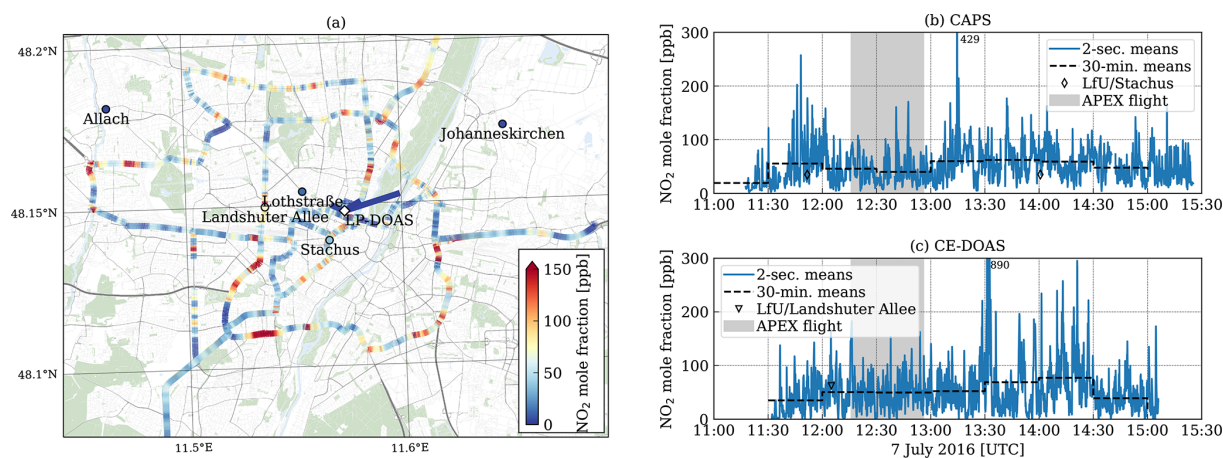
Figure 4. (a) Map of NO$_2$ mole fractions measured by LMU and MPIC vehicles in the afternoon. Locations of the LfU monitoring stations are shown as circles colored by the mean afternoon NO$_2$ mole fraction. Panels **(b)** and **(c)** show the time series of NO$_2$ mole fractions measured by the CAPS and CE-DOAS instruments on the LMU and MPIC vehicles, respectively. Map data from © OpenStreetMap contributors 2021. Distributed under the Open Data Commons Open Database License (ODbL) v1.0.
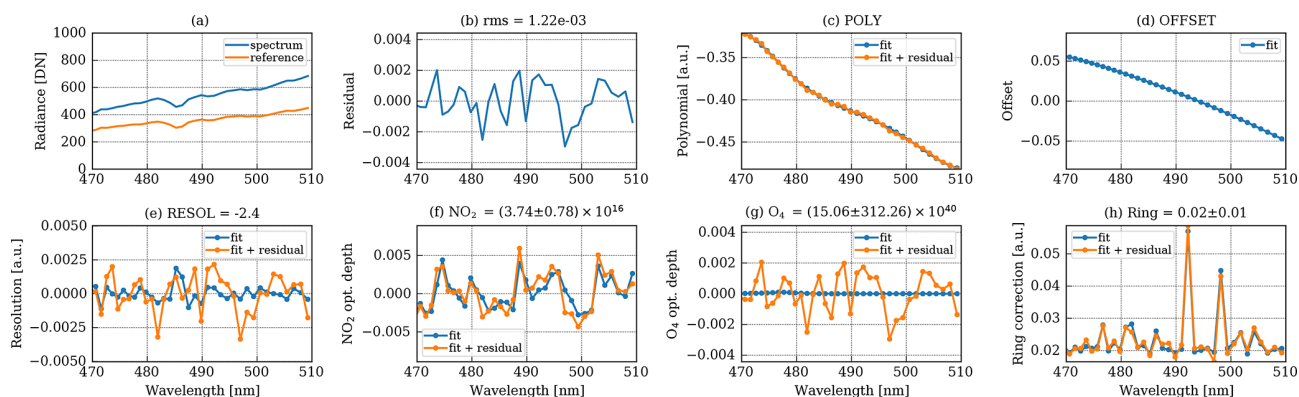

Figure 5. Example of DOAS retrieval for APEX stripe no. 2 inside the NO$_2$ plume of the Heizkraftwerk Süd power plant at across- and along-track positions of 42 and 314, respectively: **(a)** APEX measurement spectrum and reference spectrum, **(b)** residual, **(c)** fitted polynomial, **(d)** fitted offset, **(e)** resolution cross section, **(f)** NO$_2$ optical depth, **(g)** O$_4$ optical depth, and **(h)** Ring pseudo cross section.

mobile measurements and measuring stations for these data can be found in Zhu et al. (2020).

3.3 APEX NO$_2$ observations

3.3.1 APEX NO$_2$ retrieval algorithm

The true color images of the four APEX stripes are shown in Fig. S3. The stripes were mostly cloud-free, with only a small cumulus cloud on the western edge of the second stripe.

The spectral calibration was much more stable than on other flights investigated by Kuhlmann et al. (2016), likely because the measurements were conducted after the long transfer flight from Zurich to Munich prior to the measurements, allowing the system to reach a stable pressure and temperature state. The in-flight spectral calibration shows the known spectral smile of the APEX instrument in the across-track direction (Fig. S5a) but no strong drift during data ac-

quisition in the along-track direction (Fig. S5b). The instrument slit function is about 30 % wider in-flight than the laboratory calibration (see Sect. 2.5), which is a known but not fully understood characteristic of the APEX instrument that is likely related to stray light and vignetting (Kuhlmann et al., 2016).

Figure 5 shows an example of the DOAS analysis for an APEX pixel acquired inside the plume of the Munich South CHP plant (stripe: 2, across-track: 42, along-track: 314) with a root mean square (rms) of 1.22×10^{-3} and an NO$_2$ dSCD of $621 \pm 130 \, \mu mol \, m^{-2}$.

The distributions of rms, dSCDs, HCRFs, AMFs, and VCDs are shown in Fig. 6 for the second stripe. The distributions for the other APEX stripes are shown in Figs. S6–S8.

For all stripes, rms values do not vary strongly spatially, ranging from 0.49 to 1.00×10^{-3} (5th to 95th percentiles) with a mean value of 0.73×10^{-3}. The values are smallest in
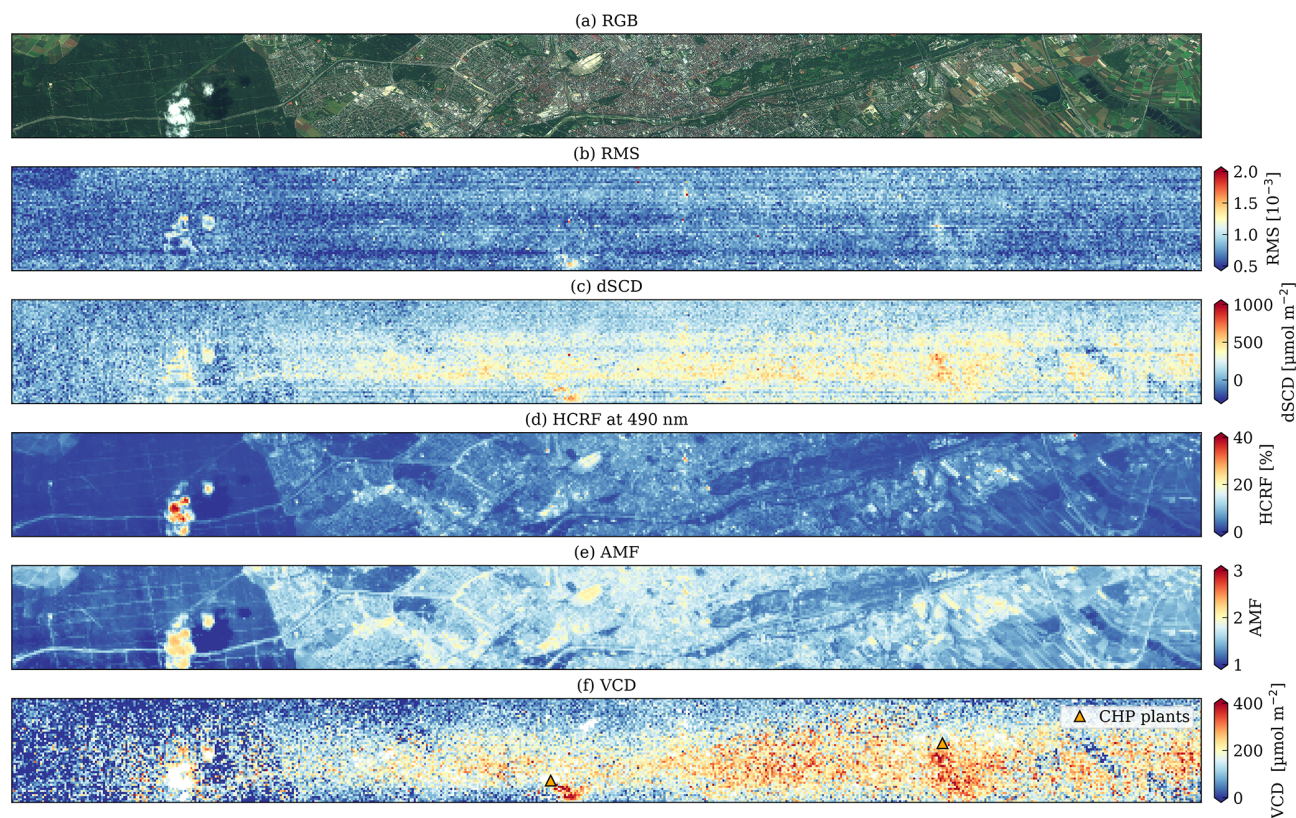
Figure 6. (a) True color image, **(b)** rms, **(c)** NO$_2$ differential slant column densities (dSCDs), **(d)** hemispheric–conical reflectance factors (HCRFs), **(e)** air mass factors (AMFs), and **(f)** NO$_2$ vertical column densities (VCDs) of the second APEX stripe (see Fig. 1).

the area used for computing the reference spectra (Fig. 6a). The rms values are highest over very bright surfaces and increase with distance from the reference area. This dependency on along-track position is likely caused by a mismatch in spectral calibrations between the reference and measurement spectra that increases with distance from the reference area. The rms values also vary in the across-track direction, where positions have a higher rms than others, also likely caused by small differences in the spectral calibration.

The NO$_2$ dSCDs show no clear spatial pattern, but values are highest in the middle over the city and lowest on the right-hand side over the forest used as the reference area (Fig. 6b). The average dSCD is 178 µmol m^{-2}, but values range between -71 and 417 µmol m^{-2} (5th to 95th percentiles).

HCRFs at 490 nm in the APEX product varied over the city from 0.02 to 0.12 (5th to 95th percentiles), with a mean of 0.06. The HCRFs were smaller, with an average value of 0.03 (range: 0.01–0.06) over the forest in the west of the city, which was used as a reference area for the DOAS analysis. The AMFs depend mainly on HCRFs and range between 1.1 and 1.9 with an average of 1.5 (Fig. 6d).

The NO$_2$ VCDs computed from dSCDs and VCDs (Eq. 2) have an average of 115 µmol m^{-2} and range from -37 to 294 µmol m^{-2} (5th to 95th percentiles). The destriping algorithm successfully removes the stripes visible in the dSCDs

(Fig. 6e). The destriped VCD field shows clearer features, such as two enhancements in the left and center of the stripe which match the locations of the Munich North and Munich South CHP plants.

3.3.2 APEX NO$_2$ uncertainties

The uncertainties of the VCDs were obtained from the uncertainties of dSCDs, SCD$_{ref}$, and AMFs (Eq. 3). The dSCD uncertainty was obtained directly from the DOAS fitting routine and varied between 18 and 185 µmol m^{-2} with 56 µmol m^{-2} on average.

The uncertainties in the AMFs are caused mainly by uncertainties in the surface reflectance product and the a priori NO$_2$ profile used in AMF calculations. To estimate the uncertainty of the APEX surface reflectance product, we validated the product with the 14 ASD measurements in the city center covered by the second and third APEX stripes (Figs. 1 and S9, and Table S1). Figure 7 shows two examples of HCRF spectra over a dark and bright surface. APEX and ASD HCRF agree very well at 490 nm, with a correlation coefficient of 0.99, but the APEX product tends to underestimate high reflectances (slope: 1.21, intercept: -0.02). The root mean square difference (RMSD) between APEX and ASD HCRFs is 0.014 considering only ASD values smaller
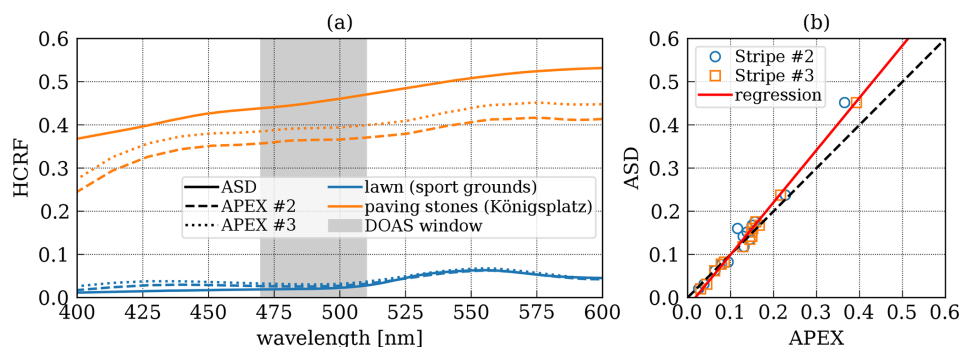
Figure 7. (a) APEX and ASD HCRF spectra for a dark and bright surface. **(b)** Scatter plot comparing APEX and ASD at 490 nm over all 14 targets. The regression line has a slope of 1.211 and an intercept of −0.022. The correlation coefficient is 0.99.
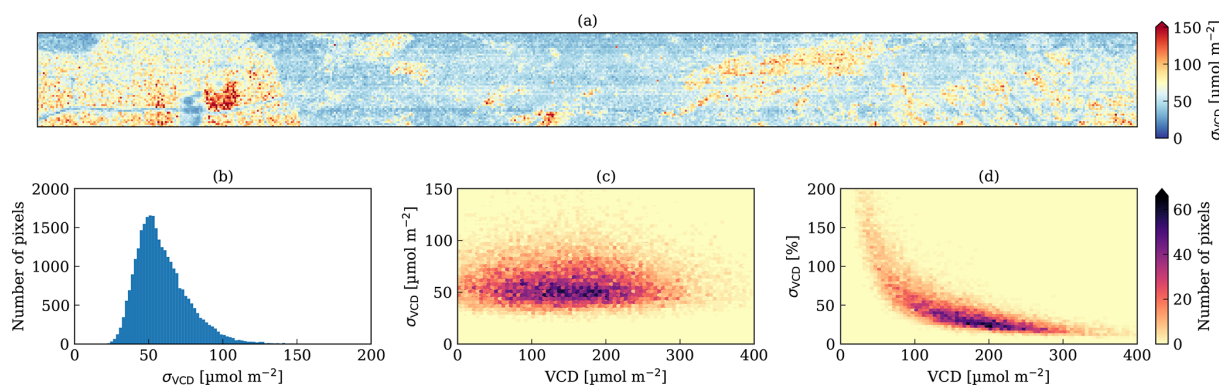

Figure 8. Estimated uncertainty of NO$_2$ VCDs for the second APEX stripe showing **(a)** the spatial distribution (see Fig. 1) and **(b)** the distribution of uncertainties and the dependency on the NO$_2$ VCDs of the **(c)** absolute and **(d)** relative uncertainties.

than 0.30, which is a relative uncertainty of about 23 % for the mean HCRF over the city (HCRF = 0.06). We computed the 1σ uncertainties of the AMFs using an uncertainty of 0.014 in HCRFs, which results in AMF uncertainties of 0.15 and 0.08 for HCRFs of 0.03 and 0.06, respectively.

The uncertainties in the a priori NO$_2$ profiles translate to about 10 % uncertainty in AMFs for satellite NO$_2$ products (e.g., Boersma et al., 2011). In our study, the a priori NO$_2$ profile was obtained from the MAX-DOAS instrument on the MIM rooftop, which should provide a representative profile for the city above building level. Since the instrument is not sensitive to near-surface NO$_2$, we analyzed the impact of the NO$_2$ profile sensitivity by replacing the mole fraction in the lowest layer (0–200 m) with values ranging from 0 to 100 ppbv. We find that the corresponding AMF uncertainty is smaller than 0.10 for LERs larger than 0.20 and up to 0.16 for a black surface (LER = 0.00).

The total AMF uncertainties are obtained as a sum of variances of the individual components (surface reflectance and the a priori NO$_2$ profile). We calculated that AMF uncertainties decrease from 0.40 to 0.10 when LERs increase from 0.00 to 0.05 and are constant at 0.10 when LERs are larger than 0.05. Uncertainties might be somewhat larger because

uncertainties in the aerosol profiles are not taken into account.

The uncertainty of the reference slant column density (SCD$_{ref}$) was estimated to be about 25 % considering the uncertainty of the VCDs retrieved from the Mini MAX-DOAS ($\sigma_{SCD} < 15$ %) and the uncertainty of the AMFs averaged over the forest used as the reference area ($\sigma_{AMF} \approx 0.13$).

The VCD uncertainties were computed from Eq. (3). The uncertainty is dominated by the dSCD uncertainty that accounts for 87 % of total uncertainty due to the low signal-to-noise ratio of the APEX measurements. The second-most important term is the AMF uncertainty accounting for 12 % of the total uncertainty, while the uncertainty of the reference SCD is small compared to the other two components. Figure 8a shows the estimated uncertainties for the second stripe. The uncertainties are highest over dark surfaces (forest, parks, and water surfaces), because the uncertainty inversely depends on AMFs (Eq. 3). The uncertainty ranges from 34 to 86 μmol m^{-2} (5th–95th percentiles), with an average of 56 μmol m^{-2} (Fig. 8b). Since the uncertainty depends on VCDs, uncertainties slightly increase with VCDs (Fig. 8c).
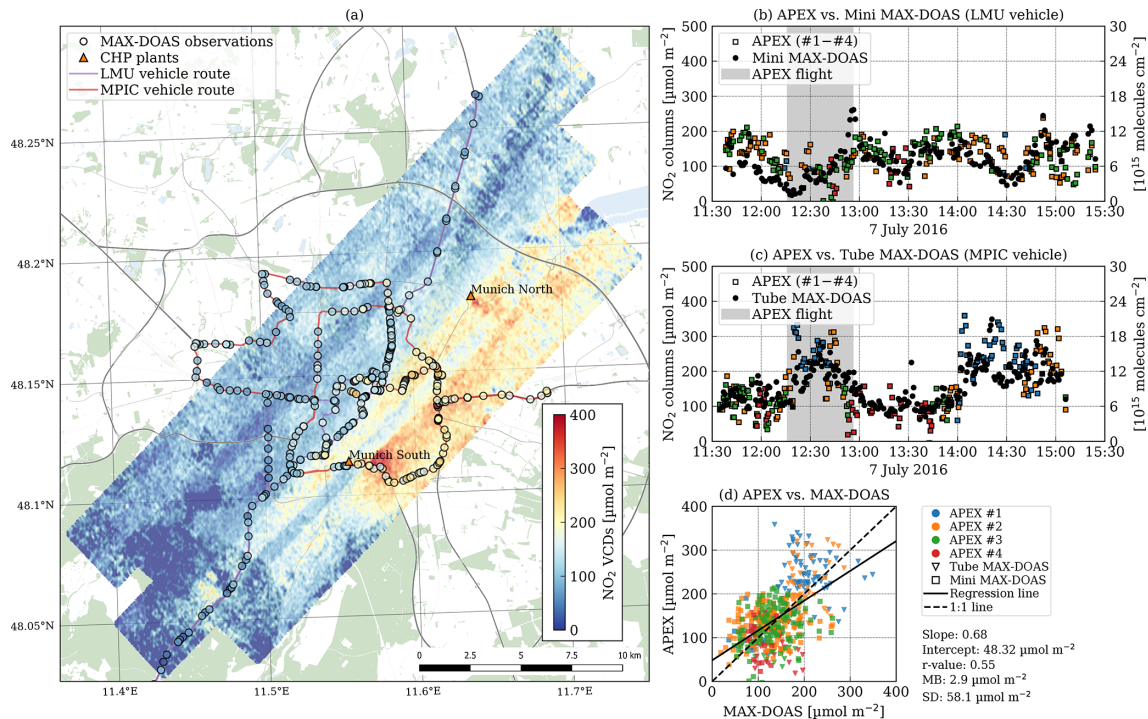
Figure 9. **(a)** Map NO$_2$ VCDs from APEX and mobile MAX-DOAS measurements on 7 July 2016 (afternoon). **(b, c)** Time series of spatially co-located APEX and **(b)** Mini MAX-DOAS and **(c)** Tube MAX-DOAS VCDs. **(d)** Scatter plot showing MAX-DOAS and APEX NO$_2$ VCDs for spatially co-located observations. Map data from © OpenStreetMap contributors 2021. Distributed under the Open Data Commons Open Database License (ODbL) v1.0.

3.3.3 APEX NO$_2$ map

Figure 9a shows the map of NO$_2$ VCDs from the APEX instrument. A Gaussian smoothing filter ($\sigma \approx 50$ m) was applied to reduce spatial noise. The map shows lower values in the northwest upwind and higher values in the southeast downwind of the city center. The locations of the Munich North and Munich South CHP plants are marked by two orange triangles. The emission plumes of both CHP plants are clearly visible in the APEX data. Otherwise, no small-scale structures, such as roads, can be identified on the map.

While local enhancements related to traffic such as key intersections and highways could be identified in previous APEX campaigns (e.g., Popp et al., 2012; Tack et al., 2017), such structures are missing in Munich, likely due to the high variability in wind speed and direction resulting in strong spatial mixing. Recent model studies demonstrate that this is also partially explainable by 3D radiative transfer effects (Schwaerzel et al., 2021).

The APEX NO$_2$ product also shows artifacts near the stripe edges that are likely related to insufficient knowledge about the spectral calibration and vignetting that affect the accuracy of the instrument slit function (Kuhlmann et al., 2016). The NO$_2$ map also shows unrealistic low values over water surfaces that have also been noticed by Tack et al. (2017).

3.4 Comparison of APEX and MAX-DOAS observations

Figure 9b and c show the time series of spatially but not temporally collocated APEX and MAX-DOAS NO$_2$ VCDs, which were obtained by averaging the APEX values along the vehicle paths ± 30 and ± 15 s for the Mini and Tube MAX-DOAS, respectively. The LMU vehicle drove along the magenta line (Fig. 9a), leaving the urban area in the southeast and northwest. The time series shows local NO$_2$ minima when the vehicle was at the southwestern border of the APEX map at 12:20 and 14:35 UTC and at the northwestern border of the APEX map at 13:25 UTC. The MPIC vehicle was driving in a counterclockwise direction around the city center along the red line in Fig. 9a. NO$_2$ VCDs were highest when the vehicle was located in the eastern part of the city (12:30 and 14:30 UTC). A map showing the time labels is provided in Fig. S10.

In total, 518 co-located APEX and MAX-DOAS observations are available. APEX and MAX-DOAS NO$_2$ VCDs agree with a moderate correlation coefficient r of 0.55. The regression line has a slope of 0.68 and an intercept of 48.3 μmol m^{-2}. Furthermore, the mean bias (MB) computed from the differences between APEX and MAX-DOAS measurements is close to zero, at 2.9 μmol m^{-2}. The standard deviation (SD) of the differences is 58.1 μmol m^{-2}. The dis-
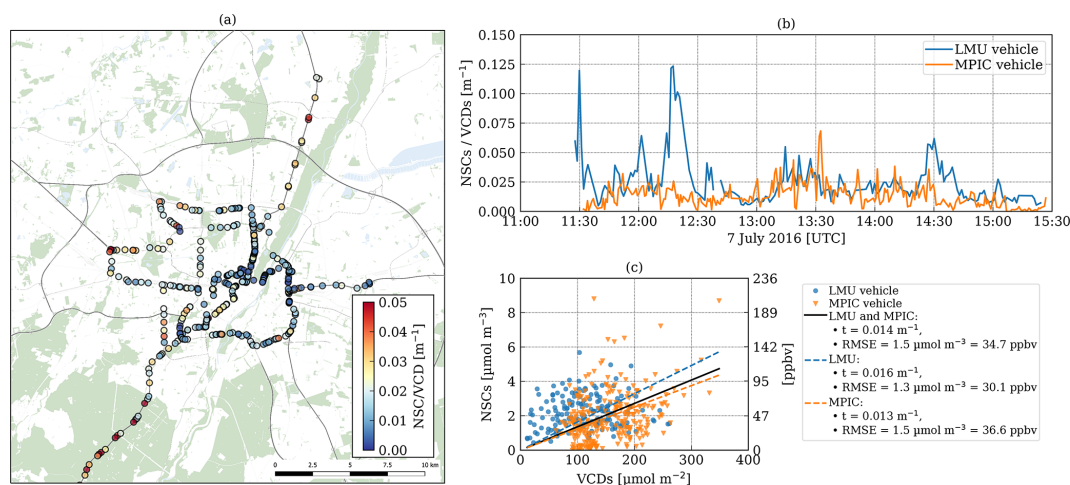
Figure 10. (a) Map of ratios of NO$_2$ NSCs (µmol m^{-3}) to VCDs (µmol m^{-2}) measured by in situ monitors and MAX-DOAS on board the LMU and MPIC vehicles. **(b)** The time series of ratios measured with the two vehicles and **(c)** a scatter plot of NSCs and VCDs. Map data from © OpenStreetMap contributors 2021. Distributed under the Open Data Commons Open Database License (ODbL) v1.0.

crepancy between airborne and ground-based observations is largely explainable by the relatively high uncertainty of individual APEX and MAX-DOAS NO$_2$ VCDs (i.e., APEX uncertainties were approximately 60 µmol m^{-2}). In addition, airborne and ground-based instruments do not measure exactly the same air mass due to different viewing directions and different measurement times. Furthermore, the vertical sensitivity to NO$_2$ is different for APEX and MAX-DOAS, so that inconsistent assumptions about the vertical profile of NO$_2$ affects the comparison. It should be noted that APEX and MAX-DOAS observations are not fully independent, because the APEX NO$_2$ retrieval algorithm uses MAX-DOAS measurements as VCD$_{ref}$.

3.5 Relationship between near-surface concentrations and vertical column densities

Airborne NO$_2$ maps from imaging remote sensing instruments can be valuable for studying the spatial distribution of air pollutants in a city. However, to access the impact of NO$_2$ on human health, it is necessary to transfer VCDs to NSCs using a transfer parameter t such that

$$\text{NSC} = t \cdot \text{VCD}. \tag{4}$$

The parameter t (m^{-1}) is the ratio of NSCs (µmol m^{-3}) and VCDs (µmol m^{-2}). It depends on the shape of the vertical NO$_2$ profile, which varies in space and time with local NO$_x$ emissions, meteorological factors such as wind speed and vertical mixing, NO$_x$ chemistry, and NO$_2$ advected from the surroundings.

In the MuNIC campaign, both NSCs and VCDs were measured simultaneously by the in situ monitors and the MAX-DOAS instruments on board the MPIC and LMU vehicles. It is therefore possible to calculate the ratio of NSCs and

VCDs and to study the spatial variability of the transfer parameter. Figure 10a shows the spatial distribution of the ratio on 7 July 2016 (afternoon). The ratios are highest outside the city plume, where VCDs are low but NO$_2$ NSCs on the roads are still high. In contrast, ratios are small inside the plume, where both NSCs and VCDs are high but NSCs make up a smaller fraction of the total column. The ratios vary strongly along the roads due to the highly variable NO$_2$ concentrations due to traffic emissions. We did not measure NSCs away from roads, but since NSCs tend to be smaller away from roads and VCDs do not show much spatial variability, we expect lower and less variable values there.

A constant transfer parameter can be obtained by fitting the NSC on the VCD measurements using Eq. (4). Figure 10c shows the scatter plot and the fitted lines. The parameter t is 0.014 m^{-1} when using measurements from both the MPIC and LMU vehicles. The RMSE is large at 1.5 µmol m^{-3} or 34.7 ppbv, showing that estimated NSCs from airborne observations would be highly uncertain. The estimate can likely be improved when considering additional factors such as local emissions, and emissions upstream of a location as NSCs are very sensitive to local emissions, while VCDs from MAX-DOAS and airborne imagers are more representative of larger areas (Irie et al., 2011; Schwaerzel et al., 2020, 2021).

3.6 NO$_x$ and CO$_2$ emissions of point sources

The two largest point sources in the city are the Munich North CHP plant and Munich South CHP plant (see Fig. 1). For 2016, Munich North reported CO$_2$ and NO$_x$ mean emissions of 80 kg CO$_2$ s^{-1} and 53 g NO$_2$ s^{-1}, respectively, and Munich South reported 26 kg CO$_2$ s^{-1} and 14 g NO$_2$ s^{-1} (European Environment Agency, 2021). Since instantaneous emissions usually differ from annual means, we calculated
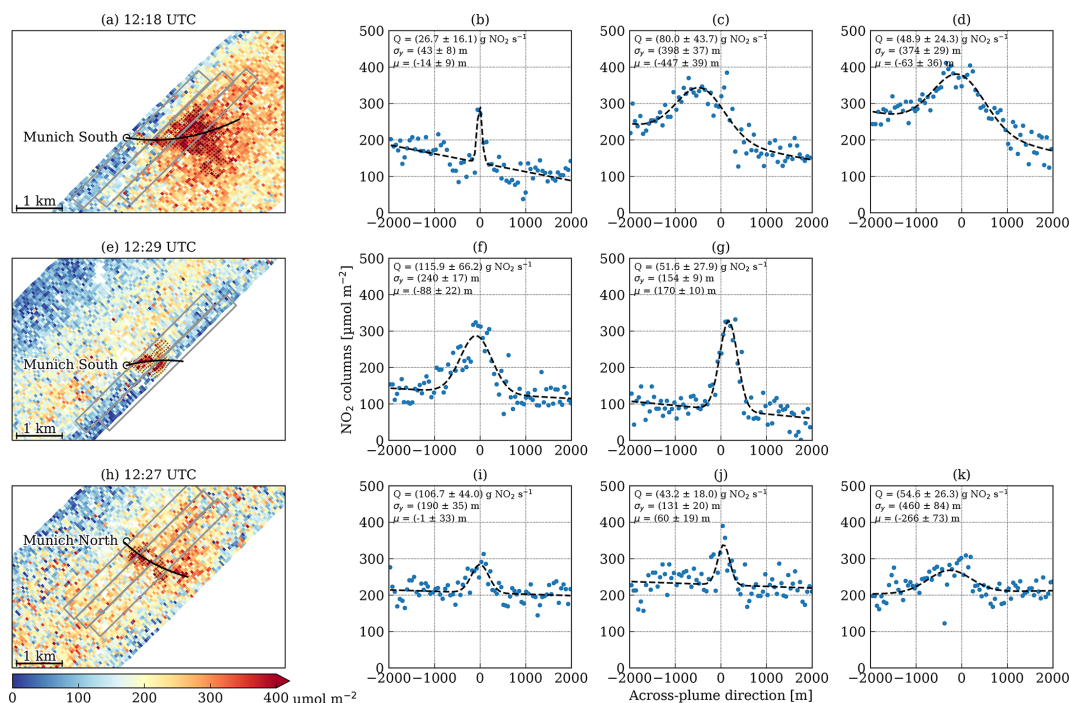
Figure 11. (**a, e, h**) APEX NO$_2$ maps with emission plumes (black dots) of the Munich South and Munich North CHP plants. The center line of the plume is shown as a black curve. (**b–d, f, g, i–k**) APEX NO$_2$ VCDs averaged in the across-track direction within gray boxes shown in the maps and a Gaussian curve fitted to the observations (dashed line).

the instantaneous emissions of Munich South using the natural gas consumption provided by the operating Stadtwerke München (SWM) using a conversion factor of 1.9225 kg CO$_2$ per Nm^3 natural gas (U.S. EPA, 2016) and the mass ratio of annual CO$_2$ and NO$_x$ emissions. The computed emissions are 44.2 kg CO$_2$ s^{-1} and 23.1 g NO$_2$ s^{-1}, which is about 70 % higher than annual means, and only vary slightly by ± 1.3 kg CO$_2$ s^{-1} and ± 0.7 g NO$_2$ s^{-1} between 09:30 and 14:00 UTC on 7 July 2016.

CO$_2$ and NO$_x$ emissions can be estimated from CO$_2$ and NO$_2$ observations. APEX flew once over Munich North at 12:27 UTC (stripe 2) and twice over Munich South at 12:18 and 12:29 UTC (stripes 1 and 2). The NO$_2$ emission plumes of the two CHP plants are visible in the APEX observations (Fig. 11a, e, and h). In addition, the CO$_2$ plume of Munich South was observed by the FTIR spectrometers (Fig. 12).

Figure 12a shows the setup of the two FTIR spectrometers where the instruments can observe XCO$_2$ upwind and downwind of the plume. The XCO$_2$ time series of the instruments is shown in Fig. 12c. The KIT instrument frequently observed the CO$_2$ enhancement of the CHP plant plume downwind of the source, while the TUM instrument observed the upwind values. Since the plume location meanders depending on wind speed and direction, the line of sight of the FTIR instrument will not always include the plume. In fact, during the APEX measurements, the FTIR instruments did not capture any CO$_2$ enhancements, because the line of sight followed the Sun towards the west while the wind carried the plume towards the southeast. Figure 12b shows the APEX NO$_2$ field overlaid with the lines of sight of the two FTIR spectrometers, confirming that the plume was not in the instrument's field of view at APEX overpass time.

3.6.1   NO$_x$ emissions

The NO$_x$ emissions of the Munich North and Munich South CHP plants were estimated from the APEX observations using a plume detection algorithm and mass-balance approach implemented as part of a Python package for "Data-driven Emission Quantification" (Kuhlmann, 2021a; Kuhlmann et al., 2021). The NO$_x$ emissions Q were obtained by computing the cross-sectional flux as

$$Q = f(x) \cdot q(x) \cdot u(x) \cdot \cos(\alpha(x)), \qquad (5)$$

where x is the along-plume coordinate, f is the NO$_2$: NO$_x$ conversion factor, q is the line density, and $u \cos(\alpha)$ is the wind speed normal to the cross section used for computing the line density. The line density was computed by fitting a Gaussian curve to the along-track NO$_2$ VCDs:

$$\text{VCD}(y) = \frac{q}{\sqrt{2\pi}\sigma} \exp\left(-\frac{(y-\mu)^2}{2\sigma^2}\right) + m\,y + b, \qquad (6)$$

where y is the across-plume coordinate, μ is a shift, and σ is the standard width. The NO$_2$ background was approximated by a linear function with slope m and intercept b.
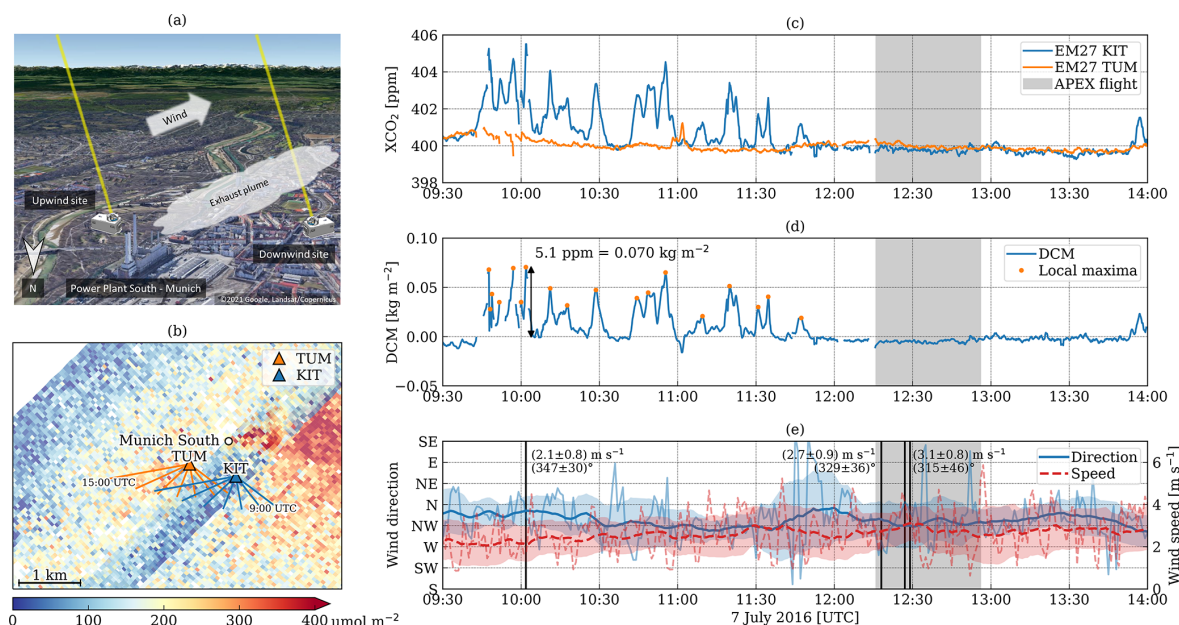
Figure 12. (a) The setup of the two FTIR spectrometers at Munich South. **(b)** APEX NO_2 map showing the NO_2 emission plume and the locations of the FTIR spectrometers. The lines are hourly lines of sight below 1100 m above ground. **(c)** XCO_2 time series and **(d)** differential CO_2 measurements (DCM) for the two instruments. **(e)** Wind speed and direction measured every minute on the LMU rooftop at 30 m above ground (thin lines). In addition, a 30 min rolling average was applied to the time series (thick lines). The shaded area shows the 1σ temporal variability within 30 min. Vertical lines show times with the largest CO_2 peak and NO_2 measurements by the APEX instrument. The numbers are 30 min mean wind speed and direction.

To compute the across- and along-plume coordinates, the location and extent of the NO_2 emission plumes were determined using a plume detection algorithm, which detects pixels where the local mean is significantly enhanced above the background (Kuhlmann et al., 2019, 2021). The local mean was computed using a Gaussian filter with a standard width of 0.75 pixels. The background was computed as the median of 100 adjacent pixels in the along-track direction to avoid issues with across-track stripes. A 2D curve was then fitted to the detected pixels to describe the center line of the plume. x and y coordinates were computed as arc length from the source and the distance from the curve, respectively. The tangent of the curve was used to determine the wind direction that is used to compute the angle α.

A critical input for estimating the emissions is the wind speed profile, which determines the height of the plume due to plume rise and the wind speed inside the plume. Figure 12e shows the time series of wind speeds and directions measured on the MIM's rooftop at 30 m above ground. The wind speed measured every minute shows high variability with a standard deviation of about 0.9 m s^{-1} for 30 min rolling means. Since MIM's rooftop is more than 3 km away from the stacks, the highly variable wind measurements are not well suited as input for estimating emissions. We therefore used the simulations from the COSMO-1 and COSMO-7 analysis products. The 10 m wind fields and vertical profiles are shown in Figs. S11 and S12. Since the COSMO-1 model with about

1 km resolution shows small convective cells whose locations are determined by a stochastic process, we average 6×6 grid cells to obtain an average wind profile and its uncertainty at the stack locations.

The plume height needs to consider plume rise that can be computed from heat emissions, wind speed at the stack, and the dispersion category (VDI – Fachbereich Umweltmeteorologie, 1985). The Munich South CHP plant has three stacks ($H = 90$ m), for which we use heat emissions of 70 MW obtained from the operator. The dispersion category was already determined as very unstable (category: V) in Sect. 3.1. The wind speed at the height of the stacks is calculated from the COSMO-1 profiles as 2.5 ± 1.3 m s^{-1} at 10:00 UTC. The plume height starts at the 90 m stack and rises quickly to a maximum height of 845 m at about 1580 m downstream of the stack (Fig. S13). We use the wind speed taken from the COSMO-1 profiles at the height of the plume to estimate NO_x emissions. The distance from the plume is given by the arc length of the center lines. We assume the same heat emissions and stack height to estimate the plume rise for the Munich North CHP plant.

The $NO_2 : NO_x$ conversion factor f was computed using an NO lifetime of 0.3 h for dispersion category V (VDI – Fachbereich Umweltmeteorologie, 2009, Sect. 10.2) and a residence time, which was computed using the distance from the source to the cross section and the wind speed.

The uncertainties were computed using the uncertainty of the NO$_2$ VCDs in the Gaussian curve fit and the uncertainty of the wind speed from the spatial standard deviation in the COSMO-1 model. The uncertainty of the wind speed affects the uncertainty directly in Eq. (5) and indirectly due to its impact on the NO$_2$: NO$_x$ conversion factor. The uncertainty of the conversion factor is also affected by the uncertainty of the NO lifetime, which is difficult to quantify as it requires, for example, detailed simulations of the NO$_x$ chemistry in the turbulent emission plume. For the sake of simplicity, we assume an uncertainty of 50 % in this study. Since the uncertainty of wind speed dominates the total uncertainty, additional factors were not included in the uncertainty calculations.

Figure 11a, e, and h show the three APEX observations at Munich North and Munich South with the detected pixels (black dots) and center lines. Line densities were computed by averaging five lines in the across-track direction within ±2000 m from the center line indicated by the rectangular boxes in the figure. The input parameters and the estimated NO$_x$ emissions are shown in Table S2. For Munich South, estimated NO$_x$ emissions range from 26.7 to 115.9 g NO$_2$ s^{-1}, with an average of 64.6 ± 20.3 g NO$_2$ s^{-1}, i.e., a relative uncertainty of 31 %, where the uncertainty is the standard error of the mean. For Munich North, only three line densities could be computed, resulting in emissions ranging from 43.2 to 106.7 g NO$_2$ s^{-1} (average: 68.2±24.8 g NO$_2$ s^{-1}).

3.6.2 CO$_2$ emissions

The CO$_2$ emission strength can be estimated from the differential column measurements (DCMs), i.e., the difference between the upstream and downstream observations, which represents the enhancement due to the source (Fig. 12a, Chen et al., 2017). If we assume that the emission plume can be approximated by a Gaussian plume model and that the local peaks in the DCM time series occur when the plume center moves over the downwind station (i.e., they correspond to the maxima in the Gaussian), the source strength Q would be given by

$$Q = \sqrt{2\pi}\, u(x)\, \sigma_y(x)\, \mathrm{DCM_{max}}(x), \qquad (7)$$

where u is the wind speed inside the plume, σ_y is the horizontal width of the plume, and DCM$_{max}$ is the CO$_2$ enhancement in the center of the Gaussian plume. Note that u, σ_y, and DCM$_{max}$ depend on the distance from the source x.

Figure 12d shows the time series of DCMs measured on 7 July 2016. In total, we identified 18 local maxima using a standard peak finding algorithm of the SciPy library (Virtanen et al., 2020, Version 1.4.1) for estimating CO$_2$ emissions. The highest DCM was measured at 10:02 UTC with 5.1 ppm, which is converted to a mass column density of 0.070 kg m^{-2}.

The wind speed was taken from the COSMO-1 profiles to compute plume rise and the distance of the plume from the stack at the slant line of sight of the FTIR instrument

(Fig. S13). The KIT EM27 spectrometer was located 582 m downstream of the stack. At 10:02 UTC, the line of sight of the instrument and the plume height intersect at a height of 615$^{+274}_{-177}$ m. Consequently, the distance from the source x is 915$^{+485}_{-114}$ m downstream of the source. The dispersion coefficients were computed based on VDI guidelines, which assumes constant coefficients above 180 m. It is computed by an empirical equation $\sigma_y(x) = F \cdot x^f$ with $F = 0.671$ and $f = 0.903$ for dispersion category V. Therefore, $\sigma_y(x)$ ranges were computed as 317$^{+85}_{-36}$ m at the intersection. The standard deviations were computed from the spatial variability in COSMO-1 wind speeds.

The CO$_2$ emissions were then computed by Eq. (7) using a wind speed in the plume center of 2.4 ± 0.7 at 615 m above ground, which results in emissions of 134 ± 49 kg CO$_2$ s^{-1}. The uncertainty was estimated using a DCM uncertainty of 0.1 ppm for 1 min averages (Chen et al., 2016) as well as the uncertainties of $u(x)$ and $\sigma_y(x)$. The uncertainty budget is dominated by the uncertainty in the wind speed that accounts for 72 % of the total uncertainty. The uncertainty of the dispersion coefficient σ_y accounts for 27 % of the total uncertainty, which also depends on the uncertainty of the wind speed, while the uncertainty of the DCM measurements is negligible.

The emissions were computed for all 18 peaks, and results are shown in Table S3. The estimated CO$_2$ emissions vary strongly, ranging from 38 to 134 kg CO$_2$ s^{-1}. The mean and standard error of all 18 estimates are 81.2 ± 8.6 kg CO$_2$ s^{-1}.

3.6.3 Comparison with reported emissions

CO$_2$ and NO$_x$ emissions of the Munich South CHP plant were estimated as 81.2 ± 8.6 kg CO$_2$ s^{-1} and 64.6 ± 20.3 g NO$_2$ s^{-1}, significantly higher than the emissions of 44.2 ± 1.3 kg CO$_2$ s^{-1} and 23.1 ± 0.7 g NO$_2$ s^{-1} computed from fuel consumption. The NO$_x$-to-CO$_2$ emission ratios are similar between reported and estimated emissions.

The main reason that the estimated emissions are higher than the reported values is likely due to the unstable and highly turbulent atmospheric boundary layer resulting in low and highly variable wind speeds, which makes applying mass-balance approaches challenging for estimating emissions. On the one hand, uncertainties are large, because accurate knowledge of the wind speed is critical, as it not only affects the computation of the flux, but also the calculation of plume rise, dispersion coefficient, and NO lifetime. On the other hand, mass-balance approaches assume stationary conditions, which is not very accurate, especially in turbulent flow conditions.

The method applied to estimating CO$_2$ emissions from the FTIR measurements assumed that the plume can be approximated by a Gaussian plume model and that the local maxima are the maxima in the vertically integrated Gaussian plume. However, maxima in the time series also occur when the wind speed is below the average. As a result, the

assumption of an average wind speed would overestimate the CO_2 emissions. The individual COSMO-1 wind profiles (Fig. S12) show that the lower wind speeds would halve the values, which would also lead to a halving of estimated CO_2 emissions much more consistent with our estimate from fuel consumption. The turbulent flow will also result in puff-like structures in the plume, where CO_2 values are locally enhanced or reduced compared to a Gaussian model, which will either overestimate or underestimate emissions. Furthermore, it is possible that only the edge of the plume passes briefly through the line of sight, which would result in a local maximum but underestimate the emissions. To limit the impact on our estimate, we have estimated emissions for all local peaks in the time series, yet our estimates are still likely to be too high, as the algorithm for identifying peaks does not account for minor peaks.

The computation of the cross-sectional flux for estimating NO_x emissions from the APEX NO_2 observations is also limited by the turbulent flow, because the emission plumes are already very wide just 1 km downstream of the source, which makes it difficult to determine the center line of the plume and the angle between APEX stripe and wind vector. The wind profiles from the simulations and the measurements are less consistent in the afternoon, and the COSMO-1 wind profiles might be overestimated (Fig. S12), which could explain the overestimated NO_x emissions. In addition, the estimation of NO_x emissions is sensitive to the NO_2-to-NO_x conversion factor f, which in turn depends on NO lifetime and wind speed. For turbulent flow, the residence time is likely longer than the value computed from mean wind speed and distance from the source, resulting in a smaller conversion factor and consequently lower estimated NO_x emissions. Finally, it should also be noted that NO lifetime given by the VDI guidelines might not be sufficiently accurate for conditions on the campaign day.

4 Conclusions

In this paper, we presented results from the MuNIC measurement campaign conducted in July 2016 in Munich. The campaign measured NO_2 near-surface concentrations (NSCs) and vertical column densities (VCDs) with stationary, mobile, and airborne in situ and remote sensing instruments. A central element of the campaign was a measurement flight with the APEX imaging spectrometer mapping the spatial distribution of NO_2 VCDs on the afternoon of 7 July 2016.

Our results confirm that airborne imaging remote sensing is suited for spatial mapping of NO_2 VCDs and the detection of emission plumes from larger point sources and cities. The obtained NO_2 VCD retrievals have a moderate correlation with mobile MAX-DOAS measurements conducted on the same afternoon ($r = 0.55$), and estimated uncertainties are similar to previous findings (e.g., Tack et al., 2017). The NO_2 map obtained from the APEX data could depict the coarse-scale NO_2 distribution with lower values upwind and higher values downwind of the city but with no strong signatures of individual sources except for the two power plants.

We observed substantial differences between VCDs and NSCs. While APEX NO_2 VCDs are not elevated along roads, NSCs show high spatial and temporal variability along roads, with the highest values in congested areas and tunnels. One reason for these differences is atmospheric mixing, but 3D radiative transfer effects were also recently found to reduce the effective spatial resolution of the ground pixels and cause random uncertainties in the presence of buildings as well as an underestimation of NO_2 VCDs due to building shadows (Schwaerzel et al., 2021).

The transfer function t required for converting VCDs to NSCs is important when using imaging remote sensing for air pollution studies. However, a constant transfer parameter, calculated as the ratio of NSC over VCD from the observations, results in a very high RMSE when NSCs would be computed from VCDs. More advanced methods (than a simple constant factor) need to be applied to convert airborne NO_2 maps to near-surface concentrations. A way forward could be to combine airborne observations with a city-scale dispersion model that links NSCs and SCDs and that also needs to consider 3D radiative transfer. The unique dataset collected in the MuNIC campaign will be important for validating such approaches.

We found that NO_x emission estimates of the two combined heat and power (CHP) plants are significantly higher than reported values, but uncertainties are high due to high variability in wind speeds during the campaign day. Wind speeds are required to compute the fluxes as well as plume rise, dispersion, and residence time that have a large impact on the estimated emissions. The estimates are also likely overestimated, because the applied mass-balance approaches assume steady-state conditions, which seems to be insufficient for convective conditions if accurate and high-resolution wind fields are not available. Nonetheless, NO_x emission estimates for Munich South are consistent with CO_2 emissions determined from two ground-based FTIR instruments.

Due to the difficulty in estimating emission from airborne imaging spectrometers under convective conditions, flying during stable conditions, i.e., higher and less variable wind speeds and directions, should be an option to reduce uncertainties in future campaigns. While conditions tend to be less convective in the early morning and late afternoon, such conditions increase other challenges, including large solar zenith angles, for which 3D radiative transfer effects can affect emission estimates (Schwaerzel et al., 2020). For the planning of future campaigns, it is therefore important to consider both illumination and wind conditions in order to obtain the best possible situation for measurements and data analyses.

References

Beelen, R., Raaschou-Nielsen, O., Stafoggia, M., Andersen, Z. J., Weinmayr, G., Hoffmann, B., Wolf, K., Samoli, E., Fischer, P., Nieuwenhuijsen, M., Vineis, P., Xun, W. W., Katsouyanni, K., Dimakopoulou, K., Oudin, A., Forsberg, B., Modig, L., Havulinna, A. S., Lanki, T., Turunen, A., Oftedal, B., Nystad, W., Nafstad, P., De Faire, U., Pedersen, N. L., Östenson, C.-G., Fratiglioni, L., Penell, J., Korek, M., Pershagen, G., Eriksen, K. T., Overvad, K., Ellermann, T., Eeftens, M., Peeters, P. H., Meliefste, K., Wang, M., Bueno-de Mesquita, B., Sugiri, D., Krämer, U., Heinrich, J., de Hoogh, K., Key, T., Peters, A., Hampel, R., Concin, H., Nagel, G., Ineichen, A., Schaffner, E., Probst-Hensch, N., Künzli, N., Schindler, C., Schikowski, T., Adam, M., Phuleria, H., Vilier, A., Clavel-Chapelon, F., Declercq, C., Grioni, S., Krogh, V., Tsai, M.-Y., Ricceri, F., Sacerdote, C., Galassi, C., Migliore, E., Ranzi, A., Cesaroni, G., Badaloni, C., Forastiere, F., Tamayo, I., Amiano, P., Dorronsoro, M., Katsoulis, M., Trichopoulou, A., Brunekreef, B., and Hoek, G.: Effects of long-term exposure to air pollution on natural-cause mortality: an analysis of 22 European cohorts within the multicentre ESCAPE project, The Lancet, 383, 785–795, https://doi.org/10.1016/S0140-6736(13)62158-3, 2014.

Beirle, S., Boersma, K. F., Platt, U., Lawrence, M. G., and Wagner, T.: Megacity Emissions and Lifetimes of Nitrogen Oxides Probed from Space, Science, 333, 1737–1739, https://doi.org/10.1126/science.1207824, 2011.

Beirle, S., Borger, C., Dörner, S., Li, A., Hu, Z., Liu, F., Wang, Y., and Wagner, T.: Pinpointing nitrogen oxide emissions from space, Sci. Adv., 5, eaax9800, https://doi.org/10.1126/sciadv.aax9800, 2019.

Berk, A., Anderson, G. P., Acharya, P. K., Bernstein, L. S., Muratov, L., Lee, J., Fox, M. J., Adler-Golden, S. M., Chetwynd, J. H., Hoke, M. L., Lockwood, R. B., Cooley, T. W., and Gardner, J. A.: MODTRAN5: a reformulated atmospheric band model with auxiliary species and practical multiple scattering options, in: Multispectral and Hyperspectral Remote Sensing Instruments and Applications II, edited by: Larar, A. M., Suzuki, M., and Tong, Q., Vol. 5655, 88–95, International Society for Optics and Photonics, SPIE, https://doi.org/10.1117/12.578758, 2005.

Bigi, A., Mueller, M., Grange, S. K., Ghermandi, G., and Hueglin, C.: Performance of NO, NO$_2$ low cost sensors and three calibration approaches within a real world application, Atmos. Meas. Tech., 11, 3717–3735, https://doi.org/10.5194/amt-11-3717-2018, 2018.

Boersma, K. F., Eskes, H. J., Dirksen, R. J., van der A, R. J., Veefkind, J. P., Stammes, P., Huijnen, V., Kleipool, Q. L., Sneep, M., Claas, J., Leitão, J., Richter, A., Zhou, Y., and Brunner, D.: An improved tropospheric NO$_2$ column retrieval algorithm for the Ozone Monitoring Instrument, Atmos. Meas. Tech., 4, 1905–1928, https://doi.org/10.5194/amt-4-1905-2011, 2011.

Brunekreef, B. and Holgate, S. T.: Air pollution and health, Lancet, 360, 1233–1242, https://doi.org/10.1016/s0140-6736(02)11274-8, 2002.

Chan, K. L., Wiegner, M., Wenig, M., and Pöhler, D.: Observations of tropospheric aerosols and NO₂ in Hong Kong over 5 years using ground based MAX-DOAS, Sci. Total Environ., 619–620, 1545–1556, https://doi.org/10.1016/j.scitotenv.2017.10.153, 2018.

Chan, K. L., Wang, Z., Ding, A., Heue, K.-P., Shen, Y., Wang, J., Zhang, F., Shi, Y., Hao, N., and Wenig, M.: MAX-DOAS measurements of tropospheric NO₂ and HCHO in Nanjing and a comparison to ozone monitoring instrument observations, Atmos. Chem. Phys., 19, 10051–10071, https://doi.org/10.5194/acp-19-10051-2019, 2019.

Chan, K. L., Wiegner, M., van Geffen, J., De Smedt, I., Alberti, C., Cheng, Z., Ye, S., and Wenig, M.: MAX-DOAS measurements of tropospheric NO₂ and HCHO in Munich and the comparison to OMI and TROPOMI satellite observations, Atmos. Meas. Tech., 13, 4499–4520, https://doi.org/10.5194/amt-13-4499-2020, 2020.

Chen, J., Viatte, C., Hedelius, J. K., Jones, T., Franklin, J. E., Parker, H., Gottlieb, E. W., Wennberg, P. O., Dubey, M. K., and Wofsy, S. C.: Differential column measurements using compact solar-tracking spectrometers, Atmos. Chem. Phys., 16, 8479–8498, https://doi.org/10.5194/acp-16-8479-2016, 2016.

Chen, J., Nguyen, H., Toja-Silva, F., Heinle, L., Hase, F., and Butz, A.: Power Plant Emission Monitoring in Munich Using Differential Column Measurements, EGU General Assembly 2017, Vienna, Austria, 23–28 April 2017, Vol. 19, EGU2017–16423, https://doi.org/10.13140/RG.2.2.31907.30247, 2017.

de Hoogh, K., Saucy, A., Shtein, A., Schwartz, J., West, E. A., Strassmann, A., Puhan, M., Röösli, M., Stafoggia, M., and Kloog, I.: Predicting Fine-Scale Daily NO₂ for 2005–2016 Incorporating OMI Satellite Data Across Switzerland, Environ. Sci. Technol., 53, 10279–10287, https://doi.org/10.1021/acs.est.9b03107, 2019.

Dietrich, F., Chen, J., Voggenreiter, B., Aigner, P., Nachtigall, N., and Reger, B.: MUCCnet: Munich Urban Carbon Column network, Atmos. Meas. Tech., 14, 1111–1126, https://doi.org/10.5194/amt-14-1111-2021, 2021.

Emde, C., Buras-Schnell, R., Kylling, A., Mayer, B., Gasteiger, J., Hamann, U., Kylling, J., Richter, B., Pause, C., Dowling, T., and Bugliaro, L.: The libRadtran software package for radiative transfer calculations (version 2.0.1), Geosci. Model Dev., 9, 1647–1672, https://doi.org/10.5194/gmd-9-1647-2016, 2016.

European Environment Agency: Air quality in Europe-2019 Report, Tech. rep., https://www.eea.europa.eu/publications/air-quality-in-europe-2019 (last access: 17 March 2022), 2019.

European Environment Agency: European Industrial Emission Portal, available at https://industry.eea.europa.eu/, last access: 23 June 2021.

Gisi, M., Hase, F., Dohe, S., Blumenstock, T., Simon, A., and Keens, A.: XCO₂-measurements with a tabletop FTS using solar absorption spectroscopy, Atmos. Meas. Tech., 5, 2969–2980, https://doi.org/10.5194/amt-5-2969-2012, 2012.

Hagemann, R., Corsmeier, U., Kottmeier, C., Rinke, R., Wieser, A., and Vogel, B.: Spatial variability of particle number concentrations and NOₓ in the Karlsruhe (Germany) area obtained with the mobile laboratory "AERO-TRAM", Atmos. Environ., 94, 341–352, https://doi.org/10.1016/j.atmosenv.2014.05.051, 2014.

Hase, F., Frey, M., Blumenstock, T., Groß, J., Kiel, M., Kohlhepp, R., Mengistu Tsidu, G., Schäfer, K., Sha, M. K., and Orphal, J.: Application of portable FTIR spectrometers for detecting greenhouse gas emissions of the major city Berlin, Atmos. Meas. Tech., 8, 3059–3068, https://doi.org/10.5194/amt-8-3059-2015, 2015.

Hedelius, J. K., Viatte, C., Wunch, D., Roehl, C. M., Toon, G. C., Chen, J., Jones, T., Wofsy, S. C., Franklin, J. E., Parker, H., Dubey, M. K., and Wennberg, P. O.: Assessment of errors and biases in retrievals of XCO₂, XCH₄, XCO, and XN₂O from a 0.5 cm⁻¹ resolution solar-viewing spectrometer, Atmos. Meas. Tech., 9, 3527–3546, https://doi.org/10.5194/amt-9-3527-2016, 2016.

Heimann, I., Bright, V. B., McLeod, M. W., Mead, M. I., Popoola, O. A. M., Stewart, G. B., and Jones, R. L.: Source attribution of air pollution by spatial scale separation using high spatial density networks of low cost air quality sensors, Atmos. Environ., 113, 10–19, https://doi.org/10.1016/j.atmosenv.2015.04.057, 2015.

Heue, K.-P., Wagner, T., Broccardo, S. P., Walter, D., Piketh, S. J., Ross, K. E., Beirle, S., and Platt, U.: Direct observation of two dimensional trace gas distributions with an airborne Imaging DOAS instrument, Atmos. Chem. Phys., 8, 6707–6717, https://doi.org/10.5194/acp-8-6707-2008, 2008.

Hueni, A., Biesemans, J., Meuleman, K., Dell'Endice, F., Schlapfer, D., Odermatt, D., Kneubuehler, M., Adriaensen, S., Kempenaers, S., Nieke, J., and Itten, K. I.: Structure, Components, and Interfaces of the Airborne Prism Experiment (APEX) Processing and Archiving Facility, IEEE Trans. Geosci. Remote Sens., 47, 29–43, https://doi.org/10.1109/TGRS.2008.2005828, 2009.

Hueni, A., Lenhard, K., Baumgartner, A., and Schaepman, M. E.: Airborne Prism Experiment Calibration Information System, IEEE Trans. Geosci. Remote Sens., 51, 5169–5180, https://doi.org/10.1109/TGRS.2013.2246575, 2013.

Hundt, P. M., Müller, M., Mangold, M., Tuzson, B., Scheidegger, P., Looser, H., Hüglin, C., and Emmenegger, L.: Mid-IR spectrometer for mobile, real-time urban NO₂ measurements, Atmos. Meas. Tech., 11, 2669–2681, https://doi.org/10.5194/amt-11-2669-2018, 2018.

Ibrahim, O., Shaiganfar, R., Sinreich, R., Stein, T., Platt, U., and Wagner, T.: Car MAX-DOAS measurements around entire cities: quantification of NOₓ emissions from the cities of Mannheim and Ludwigshafen (Germany), Atmos. Meas. Tech., 3, 709–721, https://doi.org/10.5194/amt-3-709-2010, 2010.

Irie, H., Takashima, H., Kanaya, Y., Boersma, K. F., Gast, L., Wittrock, F., Brunner, D., Zhou, Y., and Van Roozendael, M.: Eight-component retrievals from ground-based MAX-DOAS observations, Atmos. Meas. Tech., 4, 1027–1044, https://doi.org/10.5194/amt-4-1027-2011, 2011.

Karagulian, F., Barbiere, M., Kotsev, A., Spinelle, L., Gerboles, M., Lagler, F., Redon, N., Crunaire, S., and Borowiak, A.: Review of the Performance of Low-Cost Sensors for Air Quality Monitoring, Atmosphere, 10, 506, https://doi.org/10.3390/atmos10090506, 2019.

Kebabian, P. L., Herndon, S. C., and Freedman, A.: Detection of Nitrogen Dioxide by Cavity Attenuated Phase Shift Spectroscopy, Anal. Chem., 77, 724–728, https://doi.org/10.1021/ac048715y, 2005.

Kebabian, P. L., Wood, E. C., Herndon, S. C., and Freedman, A.: A Practical Alternative to Chemiluminescence-Based Detection of Nitrogen Dioxide: Cavity Attenuated Phase

Shift Spectroscopy, Environ. Sci. Technol., 42, 6040–6045, https://doi.org/10.1021/es703204j, 2008.

Kim, M., Brunner, D., and Kuhlmann, G.: Importance of satellite observations for high-resolution mapping of near-surface NO₂ by machine learning, Remote Sens. Environ., 264, 112573, https://doi.org/10.1016/j.rse.2021.112573, 2021.

Kreher, K., Van Roozendael, M., Hendrick, F., Apituley, A., Dimitropoulou, E., Frieß, U., Richter, A., Wagner, T., Lampel, J., Abuhassan, N., Ang, L., Anguas, M., Bais, A., Benavent, N., Bösch, T., Bognar, K., Borovski, A., Bruchkouski, I., Cede, A., Chan, K. L., Donner, S., Drosoglou, T., Fayt, C., Finkenzeller, H., Garcia-Nieto, D., Gielen, C., Gómez-Martín, L., Hao, N., Henzing, B., Herman, J. R., Hermans, C., Hoque, S., Irie, H., Jin, J., Johnston, P., Khayyam Butt, J., Khokhar, F., Koenig, T. K., Kuhn, J., Kumar, V., Liu, C., Ma, J., Merlaud, A., Mishra, A. K., Müller, M., Navarro-Comas, M., Ostendorf, M., Pazmino, A., Peters, E., Pinardi, G., Pinharanda, M., Piters, A., Platt, U., Postylyakov, O., Prados-Roman, C., Puentedura, O., Querel, R., Saiz-Lopez, A., Schönhardt, A., Schreier, S. F., Seyler, A., Sinha, V., Spinei, E., Strong, K., Tack, F., Tian, X., Tiefengraber, M., Tirpitz, J.-L., van Gent, J., Volkamer, R., Vrekoussis, M., Wang, S., Wang, Z., Wenig, M., Wittrock, F., Xie, P. H., Xu, J., Yela, M., Zhang, C., and Zhao, X.: Intercomparison of NO₂, O₄, O₃ and HCHO slant column measurements by MAX-DOAS and zenith-sky UV–visible spectrometers during CINDI-2, Atmos. Meas. Tech., 13, 2169–2208, https://doi.org/10.5194/amt-13-2169-2020, 2020.

Kuhlmann, G.: Data-driven emission quantification (Python package), Gitlab [code], https://gitlab.com/empa503/remote-sensing/ddeq (last access: 17 March 2022), 2021a.

Kuhlmann, G.: OMI/TROPOMI gridding algorithm, Gitlab [code], https://gitlab.com/empa503/remote-sensing/gridding-algorithm (last access: 22 February 2022), 2021b.

Kuhlmann, G.: flexDOAS – A flexible Python library for DOAS analysis, Gitlab [code], https://gitlab.com/empa503/remote-sensing/flexdoas, last access: 22 February 2022.

Kuhlmann, G., Hartl, A., Cheung, H. M., Lam, Y. F., and Wenig, M. O.: A novel gridding algorithm to create regional trace gas maps from satellite observations, Atmos. Meas. Tech., 7, 451–467, https://doi.org/10.5194/amt-7-451-2014, 2014.

Kuhlmann, G., Hueni, A., Damm, A., and Brunner, D.: An Algorithm for In-Flight Spectral Calibration of Imaging Spectrometers, Remote Sens., 8, 1017, https://doi.org/10.3390/rs8121017, 2016.

Kuhlmann, G., Broquet, G., Marshall, J., Clément, V., Löscher, A., Meijer, Y., and Brunner, D.: Detectability of CO₂ emission plumes of cities and power plants with the Copernicus Anthropogenic CO₂ Monitoring (CO2M) mission, Atmos. Meas. Tech., 12, 6695–6719, https://doi.org/10.5194/amt-12-6695-2019, 2019.

Kuhlmann, G., Henne, S., Meijer, Y., and Brunner, D.: Quantifying CO₂ Emissions of Power Plants With CO₂ and NO₂ Imaging Satellites, Front. Remote Sens., 2, 14, https://doi.org/10.3389/frsen.2021.689838, 2021.

Lawrence, J. P., Anand, J. S., Vande Hey, J. D., White, J., Leigh, R. R., Monks, P. S., and Leigh, R. J.: High-resolution measurements from the airborne Atmospheric Nitrogen Dioxide Imager (ANDI), Atmos. Meas. Tech., 8, 4735–4754, https://doi.org/10.5194/amt-8-4735-2015, 2015.

Leigh, R. J., Corlett, G. K., Frieß, U., and Monks, P. S.: Spatially resolved measurements of nitrogen dioxide in an urban environment using concurrent multi-axis differential optical absorption spectroscopy, Atmos. Chem. Phys., 7, 4751–4762, https://doi.org/10.5194/acp-7-4751-2007, 2007.

Lorente, A., Boersma, K., Eskes, H., Veefkind, J., Van Geffen, J., de Zeeuw, M., van der Gon, H. D., Beirle, S., and Krol, M.: Quantification of nitrogen oxides emissions from build-up of pollution over Paris with TROPOMI, Sci. Rep., 9, 1–10, https://doi.org/10.1038/s41598-019-56428-5, 2019.

Maiheu, B., Lefebvre, W., Walton, H., Dajnak, D., Janssen, S., Williams, M., Blyth, L., and Beevers, S.: Improved Methodologies for NO₂ Exposure Assessment in the EU, Study accomplished under the authority of the European Commission, DG-Environment under service contract 070201/2015/SER/717473/C.3, Final report, Report, 2017.

Mayer, B. and Kylling, A.: Technical note: The libRadtran software package for radiative transfer calculations – description and examples of use, Atmos. Chem. Phys., 5, 1855–1877, https://doi.org/10.5194/acp-5-1855-2005, 2005.

Mueller, M., Wagner, M., Barmpadimos, I., and Hueglin, C.: Two-week NO₂ maps for the City of Zurich, Switzerland, derived by statistical modelling utilizing data from a routine passive diffusion sampler network, Atmos. Environ., 106, 1–10, 2015.

Nowlan, C. R., Liu, X., Leitch, J. W., Chance, K., González Abad, G., Liu, C., Zoogman, P., Cole, J., Delker, T., Good, W., Murcray, F., Ruppert, L., Soo, D., Follette-Cook, M. B., Janz, S. J., Kowalewski, M. G., Loughner, C. P., Pickering, K. E., Herman, J. R., Beaver, M. R., Long, R. W., Szykman, J. J., Judd, L. M., Kelley, P., Luke, W. T., Ren, X., and Al-Saadi, J. A.: Nitrogen dioxide observations from the Geostationary Trace gas and Aerosol Sensor Optimization (GeoTASO) airborne instrument: Retrieval algorithm and measurements during DISCOVER-AQ Texas 2013, Atmos. Meas. Tech., 9, 2647–2668, https://doi.org/10.5194/amt-9-2647-2016, 2016.

Platt, U., Heue, K.-P., and Pöhler, D.: Two-and Three Dimensional Observation of Trace Gas and Aerosol Distributions by DOAS Techniques, in: Atmospheric and Biological environmental monitoring, 3–11, Springer, 2009.

Popp, C., Brunner, D., Damm, A., Van Roozendael, M., Fayt, C., and Buchmann, B.: High-resolution NO₂ remote sensing from the Airborne Prism EXperiment (APEX) imaging spectrometer, Atmos. Meas. Tech., 5, 2211–2225, https://doi.org/10.5194/amt-5-2211-2012, 2012.

Richter, R. and Schläpfer, D.: Geo-atmospheric processing of airborne imaging spectrometry data. Part 2: Atmospheric/topographic correction, Int. J. Remote Sens., 23, 2631–2649, https://doi.org/10.1080/01431160110115834, 2002.

Rodgers, C. D.: Inverse methods for atmospheric sounding: theory and practice, World Scientific Publishing, Edn. 1, Series on Atmospheric, Oceanic and Planetary Physics – Vol. 2, edited by: Taylor, F. W., World Scientific Publishing Co. Pte. Ltd., https://doi.org/10.1142/3171, 2000.

Schaepman, M. E., Jehle, M., Hueni, A., D'Odorico, P., Damm, A., Weyermann, J., Schneider, F. D., Laurent, V., Popp, C., Seidel, F. C., Lenhard, K., Gege, P., Küchler, C., Brazile, J., Kohler, P., De Vos, L., Meuleman, K., Meynart, R., Schläpfer, D., Kneubühler, M., and Itten, K. I.: Advanced radiometry measurements and Earth science applications with the Airborne Prism

Experiment (APEX), Remote Sens. Environ., 158, 207–219, https://doi.org/10.1016/j.rse.2014.11.014, 2015.

Schaepman-Strub, G., Schaepman, M., Painter, T., Dangel, S., and Martonchik, J.: Reflectance quantities in optical remote sensing-definitions and case studies, Remote Sens. Environ., 103, 27–42, https://doi.org/10.1016/j.rse.2006.03.002, 2006.

Schönhardt, A., Altube, P., Gerilowski, K., Krautwurst, S., Hartmann, J., Meier, A. C., Richter, A., and Burrows, J. P.: A wide field-of-view imaging DOAS instrument for two-dimensional trace gas mapping from aircraft, Atmos. Meas. Tech., 8, 5113–5131, https://doi.org/10.5194/amt-8-5113-2015, 2015.

Schwaerzel, M., Emde, C., Brunner, D., Morales, R., Wagner, T., Berne, A., Buchmann, B., and Kuhlmann, G.: Three-dimensional radiative transfer effects on airborne and ground-based trace gas remote sensing, Atmos. Meas. Tech., 13, 4277–4293, https://doi.org/10.5194/amt-13-4277-2020, 2020.

Schwaerzel, M., Brunner, D., Jakub, F., Emde, C., Buchmann, B., Berne, A., and Kuhlmann, G.: Impact of 3D radiative transfer on airborne NO$_2$ imaging remote sensing over cities with buildings, Atmos. Meas. Tech., 14, 6469–6482, https://doi.org/10.5194/amt-14-6469-2021, 2021.

Shaiganfar, R., Beirle, S., Sharma, M., Chauhan, A., Singh, R. P., and Wagner, T.: Estimation of NO$_x$ emissions from Delhi using Car MAX-DOAS observations and comparison with OMI satellite data, Atmos. Chem. Phys., 11, 10871–10887, https://doi.org/10.5194/acp-11-10871-2011, 2011.

Tack, F., Merlaud, A., Iordache, M.-D., Danckaert, T., Yu, H., Fayt, C., Meuleman, K., Deutsch, F., Fierens, F., and Van Roozendael, M.: High-resolution mapping of the NO$_2$ spatial distribution over Belgian urban areas based on airborne APEX remote sensing, Atmos. Meas. Tech., 10, 1665–1688, https://doi.org/10.5194/amt-10-1665-2017, 2017.

Tack, F., Merlaud, A., Meier, A. C., Vlemmix, T., Ruhtz, T., Iordache, M.-D., Ge, X., van der Wal, L., Schuettemeyer, D., Ardelean, M., Calcan, A., Constantin, D., Schönhardt, A., Meuleman, K., Richter, A., and Van Roozendael, M.: Intercomparison of four airborne imaging DOAS systems for tropospheric NO$_2$ mapping – the AROMAPEX campaign, Atmos. Meas. Tech., 12, 211–236, https://doi.org/10.5194/amt-12-211-2019, 2019.

Toja-Silva, F., Chen, J., Hachinger, S., and Hase, F.: CFD simulation of CO$_2$ dispersion from urban thermal power plant: Analysis of turbulent Schmidt number and comparison with Gaussian plume model and measurements, J. Wind Eng. Ind. Aerod., 169, 177–193, https://doi.org/10.1016/j.jweia.2017.07.015, 2017.

U.S. EPA: Greenhouse Gas Inventory Guidance – Direct Emissions from Stationary Combustion Sources, Tech. rep., https://www.epa.gov/sites/default/files/2016-03/documents/stationaryemissions_3_2016.pdf (last access: 17 March 2022), 2016.

VDI – Fachbereich Umweltmeteorologie: Dispersion of air pollutants in the atmosphere; determination of plume rise, Tech. Rep. VDI 3782 Blatt 3, VDI/DIN-Kommission Reinhaltung der Luft (KRdL) – Normenausschuss, 1985.

VDI – Fachbereich Umweltmeteorologie: Atmospheric dispersion models; Gaussian plume model for the determination of ambient air characteristics, Tech. Rep. VDI 3782 Blatt 1, VDI/DIN-Kommission Reinhaltung der Luft (KRdL) – Normenausschuss, 2009.

Virtanen, P., Gommers, R., Oliphant, T. E., Haberland, M., Reddy, T., Cournapeau, D., Burovski, E., Peterson, P., Weckesser, W., Bright, J., van der Walt, S. J., Brett, M., Wilson, J., Millman, K. J., Mayorov, N., Nelson, A. R. J., Jones, E., Kern, R., Larson, E., Carey, C. J., Polat, İ., Feng, Y., Moore, E. W., VanderPlas, J., Laxalde, D., Perktold, J., Cimrman, R., Henriksen, I., Quintero, E. A., Harris, C. R., Archibald, A. M., Ribeiro, A. H., Pedregosa, F., van Mulbregt, P., and SciPy 1.0 Contributors: SciPy 1.0: Fundamental Algorithms for Scientific Computing in Python, Nat. Meth., 17, 261–272, https://doi.org/10.1038/s41592-019-0686-2, 2020.

Wagner, T., Deutschmann, T., and Platt, U.: Determination of aerosol properties from MAX-DOAS observations of the Ring effect, Atmos. Meas. Tech., 2, 495–512, https://doi.org/10.5194/amt-2-495-2009, 2009.

Wagner, T., Ibrahim, O., Shaiganfar, R., and Platt, U.: Mobile MAX-DOAS observations of tropospheric trace gases, Atmos. Meas. Tech., 3, 129–140, https://doi.org/10.5194/amt-3-129-2010, 2010.

World Health Organization: WHO global air quality guidelines: particulate matter (PM$_{2.5}$ and PM$_{10}$), ozone, nitrogen dioxide, sulfur dioxide and carbon monoxide, World Health Organization, https://apps.who.int/iris/handle/10665/345329 (last access: 17 March 2022), 2021.

Xu, H., Bechle, M. J., Wang, M., Szpiro, A. A., Vedal, S., Bai, Y., and Marshall, J. D.: National PM$_{2.5}$ and NO$_2$ Exposure Models for China Based on Land Use Regression, Satellite Measurements, and Universal Kriging, Sci. Total Environ., 655, 423–433, https://doi.org/10.1016/j.scitotenv.2018.11.125, 2019.

Zhao, X., Marshall, J., Hachinger, S., Gerbig, C., Frey, M., Hase, F., and Chen, J.: Analysis of total column CO$_2$ and CH$_4$ measurements in Berlin with WRF-GHG, Atmos. Chem. Phys., 19, 11279–11302, https://doi.org/10.5194/acp-19-11279-2019, 2019.

Zhu, Y., Chen, J., Bi, X., Kuhlmann, G., Chan, K. L., Dietrich, F., Brunner, D., Ye, S., and Wenig, M.: Spatial and temporal representativeness of point measurements for nitrogen dioxide pollution levels in cities, Atmos. Chem. Phys., 20, 13241–13251, https://doi.org/10.5194/acp-20-13241-2020, 2020.